

Cell Systems, Volume 3

Supplemental Information

**Push-Pull and Feedback Mechanisms Can
Align Signaling System Outputs with Inputs**

Steven S. Andrews, William J. Peria, Richard C. Yu, Alejandro Colman-Lerner, and Roger Brent

Document S1. Additional supplemental material, Related to STAR Methods and Figures 1–7.

Details on using yeast experimental data to generate target dose-response curves, modeling scheme, model optimization and analysis, results for two-node topologies, results for four-node topologies, robustness of results, results based on simplified and full Henri-Michaelis-Menten kinetics, and analysis of requirements for feedback to produce linear input-output relationships.

Push-pull and feedback mechanisms can align signaling system outputs with inputs**Supplementary Information**

Steven S. Andrews, William J. Peria, Richard C. Yu, Alejandro Colman-Lerner, and Roger Brent

1.	Using yeast experimental data to generate target dose-response curves	2
1.1.	<i>Ste2^{GPCR} activity</i>	2
1.2.	<i>G-protein activity</i>	3
1.3.	<i>Fus3^{MAPK} activity</i>	3
1.4.	<i>YFP expression from PRM1 promoter</i>	4
1.5.	<i>Hill function fitting method</i>	5
1.6.	<i>Summary of Hill function fits to experimental data</i>	5
2.	Modeling scheme	6
2.1.	<i>Steady-state node activities as functions of their inputs</i>	6
2.2.	<i>Two-input control reactions (two-input arrows)</i>	10
2.3.	<i>Justification for our modeling scheme</i>	10
3.	Model optimization and analysis	13
3.1.	<i>The SWRMS fit distance</i>	13
3.2.	<i>The DoRA-score, used in preliminary work</i>	16
3.3.	<i>Optimization methods</i>	16
3.4.	<i>Akaike Information Criterion computation</i>	17
3.5.	<i>Robustness computation</i>	19
4.	Results for two-node topologies	21
4.1.	<i>Two-node topologies with single control arrows</i>	21
4.2.	<i>Robustness of two-node topologies</i>	38
4.3.	<i>Control arrows act independently</i>	39
5.	Results for four-node topologies	42
5.1.	<i>Idealized target functions</i>	42
5.2.	<i>Yeast dose-response data target functions</i>	42
6.	Robustness of results to changes in input data, fitting metric, and parameter values	44
6.1.	<i>Robustness to input data and fitting metric</i>	44
6.2.	<i>Robustness to parameter variation</i>	44
7.	Michaelis-Menten kinetics	45
7.1.	<i>Simplified Michaelis-Menten</i>	45
7.2.	<i>Full Henri-Michaelis-Menten, linear topology</i>	46
7.3.	<i>Full Henri-Michaelis-Menten, topology with negative feedback</i>	48
7.4.	<i>Full Henri-Michaelis-Menten, topology with push-pull</i>	50

8. Negative feedback can produce linear input-output relationships	52
8.1. <i>General theory</i>	52
8.2. <i>Conceptual two-node signaling system with negative feedback</i>	52
8.3. <i>A human-built example of linear input-output using negative feedback</i>	54
9. References	56

1. Using yeast experimental data to generate target dose-response curves

As the main text describes, we fit our signaling system models to produce the best possible agreement with “target” dose-response curves. In some cases, we used idealized data for the target dose-response curves. In others, we used experimental data from several measurement points of the yeast pheromone response system. This section describes the experimental data that we used to create this second set of target dose-response curves.

1.1. $Ste2^{GPCR}$ activity

Several researchers have measured the dissociation constant between $Ste2^{GPCR}$ and α -factor. (i) Jenness, Burkholder, and Hartwell (Jenness et al., 1986) quantified binding between cell-surface receptors on intact cells derived from strain 381G (see (Hartwell, 1980) for its origin) and 3H -labeled α -factor by measuring radioactivity uptake from the extracellular medium. They found an equilibrium dissociation constant of about 6 nM. Their data lay along a reasonably straight line in a Scatchard plot, suggesting non-cooperative binding. These results improved upon prior ones from the same group (Jenness et al., 1983) that were based upon impure α -factor. (ii) Blumer, Reneke, and Thorner (Blumer et al., 1988) quantified binding between receptors in membrane preparations from strain RK-5116B cells and ^{35}S -labeled α -factor, also by measuring radioactivity uptake from the solution. They found a dissociation constant of 2 nM and that the data again lay along a straight line in a Scatchard plot. (iii) Yi, Kitano, and Simon (Yi et al., 2003) quantified binding between receptors on intact cells that were isogenic derivatives of strain W303 and ^{35}S -labeled α -factor in a similar fashion. They found a dissociation constant of 6 ± 3 nM. (iv) Bajaj and co-workers (Bajaj et al., 2004) investigated binding between a fluorescent α -factor analogue and GPCR proteins from strain A232. By quantifying cell fluorescence, they found a dissociation constant of 3.7 ± 0.8 nM. Finally, experiments by one of us using fluorescent alpha factor (Bush and Colman-Lerner, unpublished) assign a K_D of 2-6 nM.

From these results, we chose for this work 5 nM as the dissociation constant between $Ste2^{GPCR}$ proteins and α -factor. This value is close to the 6 nM value found by Jenness et al., and is within the 6 ± 3 nM range found by Yi et al. It is somewhat higher than the 2 nM value found by Blumer et al., but the deviation is reasonable because these measurements were from isolated membranes rather than intact cells. Similarly, it is somewhat larger than the 3.7 ± 0.8 value found by Bajaj et al., but again the deviation seems reasonable because these researchers used data from a fluorescent α -factor analogue rather than wild-type α -factor, which may bind differently.

Based on the linear Scatchard plots of the Jenness et al. and Blumer et al. results, we assumed that binding between GPCRs and α -factor obeys simple non-cooperative kinetics. This implies: that the binding dose-response curve is a Hill function; that this Hill function’s baseline, which represents the fraction of receptors bound when there is no α -factor at all, is equal to zero; that the Hill function’s maximum value, which represents the fraction of receptors bound when there is saturating α -factor, is equal to 1; that the Hill function cooperativity parameter is equal to 1, implying non-cooperative behavior; and that the Hill function EC_{50} , which is the α -factor dose concentration when exactly half of the receptors are bound, is equal to the binding dissociation constant.

1.2. G-protein activity

We used G-protein activities from Figure 4 of Yi, Kitano, and Simon (Yi et al., 2003). They quantified G-protein dissociation by measuring Förster Resonance Energy Transfer (FRET) between CFP that is tagged to $G\alpha 1$ (Gpa1) and YFP that is tagged to $G\gamma$ (Ste18) using a bulk sample (i.e. not single cells). These data were from strain RJD-415, a bar^- derivative of a W303 reference strain. The authors presented their dose-response data with the responses scaled to range from 0 to 1. For our work, we needed to rescale these data so that they would represent the absolute fraction of G-proteins that are active as a function of pheromone dose. To do so, we needed to estimate the G-protein activity levels with no pheromone stimulation and with saturating pheromone stimulation. For the former value, we used the finding that transcription from the PRM1 promoter proceeds at 4.7% of its maximum value when there is no α -factor (see section 1.4) and presumed that this arose from the basal concentration of dissociated G-proteins. From this, we set the G-protein activity baseline to 0.047. To estimate the G-protein activity with saturating pheromone, we first noted that there are 3 times more GPCRs than G-proteins (Thomson et al., 2011) and they have similar EC_{50} s, so saturating α -factor would likely activate most G-proteins. Additionally, recent work by Bush et al. (Bush et al., 2015) shows that G-protein association is catalyzed by GPCR proteins that are not ligand-bound. With saturating α -factor, essentially all of the GPCRs would be ligand-bound, which suggests that G-protein association would be infrequent, leading to a very low population of inactive G-proteins. Based on these results, we estimated that all G-proteins would be active with saturating pheromone.

The following table shows Yi et al.'s published G-protein activity results in the "original response" column, which we measured from their figure. It also shows our rescaled values, using the above baseline and maximum response values in the "rescaled response" column. Next, we found the "Best fit Hill parameters" shown below by fitting the scaled response values with a Hill function, as described in section 1.5.

$[\alpha]$ (nM)	original response	re-scaled response	Best fit Hill parameters	
0.096	0.0256	0.071		
0.988	0.151	0.191	original	rescaled
1.94	0.267	0.301	$B = 0.04$	$B = 0.047$
4.93	0.497	0.521	$A = 1.00$	$A = 0.953$
9.92	0.756	0.768	$E = 4.95$	$E = 4.95$
19.1	0.997	0.998	$N = 1.50$	$N = 1.50$
49.5	1.02	1.015		
99.6	1.03	1.024		
954	0.995	0.995		

1.3 $Fus3^{MAPK}$ activity

To generate the $Fus3^{MAPK}$ dose-response curve, we used data from the black circles plotted in Figure S14 of Yu et al. (Yu et al., 2008). These data show the amount of phosphorylated $Fus3$ as a function of the applied pheromone dose. They are scaled so that 100% represents the maximum amount of phosphorylation of the same allelic form of the $Fus3^{MAPK}$ ($Fus3-as2$) that was observed in a comparable experiment, in the presence of a chemical inhibitor, 10 mM 4-amino-1-(tert-butyl)-3-(19-naphthylmethyl)-pyrazolo[3,4-d]pyrimidine (1-NM-PP1), which inhibits the $Fus3^{MAPK}$ kinase activity, and with the pheromone dose at a saturating level. By implication, we are assuming, under these conditions, essentially every $Fus3^{MAPK}$ monomer in the cell (Thomson et al., 2011) is phosphorylated.

We also rescaled and plotted $\text{Fus3}^{\text{MAPK}}$ data plotted in Figure 5 of Yu et al. (Yu et al., 2008). We obtained the data by quantifying phosphorylated and total protein in well-calibrated Western gel experiments (Thomson et al., 2011) using strain ACL-379 (Colman-Lerner et al., 2005), a bar1^- derivative of a W303 reference strain. The following table shows these data and the best Hill function parameters to them. Section 1.5 describes the fitting method.

$[\alpha]$ (nM)	response	Best fit Hill parameters
0	0.0848	
0.001	0.140	
0.01	0.158	$B = 0.12$
0.03	0.177	$A = 0.39$
0.1	0.160	$E = 0.62$
0.3	0.265	$N = 0.76$
1.0	0.373	
3.3	0.403	
10	0.477	
33	0.483	
100	0.500	
1000	0.512	

1.4. YFP expression from *PRM1* promoter

We used data for YFP expression from the *PRM1* promoter from the original data for the black triangles that are plotted in Figure 2a of Yu et al. (Yu et al., 2008). These data were quantified from strain ACL-379 (Colman-Lerner et al., 2005). These data show a low basal expression rate, implying that there is some expression from the *PRM1* promoter even in the absence of α -factor. To account for this, we used the response that arose with no added α -factor, which was 4.7% of the maximal response, as the baseline for our Hill function fit to the data. On the other hand, there is no good way to define the maximally active value for the gene expression rate so we decided to set it to 100%. The assumption that the total amount of a reporter gene product in a time slice reflects equilibrium occupancy of DNA regulatory elements that exist in bound and unbound states was key to quantification of DNA binding in vivo by LexA and LexA fusion proteins in “repression assays” (Brent and Ptashne, 1984; Golemis and Brent, 1992).

In the following table, the column labeled “ $\langle y \rangle / \langle r \rangle$ ” represents the raw data for the average yellow fluorescence, from pheromone-induced YFP expression, divided by the red fluorescence, from constitutive RFP expression. The next column, labeled “response,” shows our re-scaled version of the raw data, adjusted to make the Hill function maximum equal to 1.

$[\alpha]$ (nM)	$\langle y \rangle / \langle r \rangle$	response	$[\alpha]$ (nM)	$\langle y \rangle / \langle r \rangle$	response	Best fit Hill parameters
0	0.466	0.0470	0.00141	0.563	0.0571	
1E-10	0.467	0.0471	0.00260	0.582	0.0590	
1.84E-10	0.468	0.0472	0.00478	0.617	0.0627	$B = 0.047$
3.39E-10	0.480	0.0485	0.00880	0.647	0.0658	$A = 0.953$
6.23E-10	0.470	0.0475	0.0162	0.704	0.0716	$E = 2.67$
1.15E-09	0.468	0.0473	0.0298	0.753	0.0767	$N = 1.24$
2.11E-09	0.404	0.0406	0.0333	0.715	0.0728	
3.88E-09	0.438	0.0441	0.0467	0.758	0.0772	
7.14E-09	0.455	0.0459	0.0653	0.820	0.0837	

1.31E-08	0.448	0.0452	0.0915	0.873	0.0891
2.42E-08	0.466	0.0470	0.128	0.995	0.102
4.45E-08	0.462	0.0466	0.179	1.10	0.113
8.18E-08	0.748	0.0762	0.251	1.26	0.130
1.51E-07	0.664	0.0675	0.351	1.44	0.147
2.77E-07	0.476	0.0481	0.492	1.68	0.173
5.10E-07	0.475	0.0480	0.689	1.86	0.191
9.38E-07	0.478	0.0483	0.964	2.38	0.245
1.73E-06	0.478	0.0483	1.35	3.23	0.333
3.18E-06	0.471	0.0475	1.89	3.87	0.399
5.84E-06	0.475	0.0479	2.65	5.15	0.532
1.08E-05	0.471	0.0476	3.70	6.17	0.637
1.98E-05	0.471	0.0475	5.19	7.15	0.739
3.64E-05	0.479	0.0484	7.26	7.59	0.784
6.70E-05	0.480	0.0485	10.2	8.58	0.886
1.23E-04	0.474	0.0478	20.3	8.95	0.925
2.27E-04	0.488	0.0493	40.7	9.43	0.975
4.17E-04	0.510	0.0516	81.3	9.57	0.990
7.68E-04	0.529	0.0536			

1.5. Hill function fitting method

We fit Hill functions to the experimental yeast dose-response data that are described above in sections 1.2, 1.3, and 1.4 by manual optimization using Excel. We fit an initial Hill function to each data set by eye, choosing the parameters that made a graph of the Hill function agree reasonably well with a scatter plot of the experimental data. We computed the fit error by summing the squared differences between the computed Hill function and the experimental data. We then adjusted the Hill function parameters until the fit error was minimized. Results shown above are the best possible fits, up to two decimal places of accuracy for each parameter.

1.6 Summary of Hill function fits to experimental data

The following table summarizes the Hill function fits to the experimental data that are presented above. See the above sections for details.

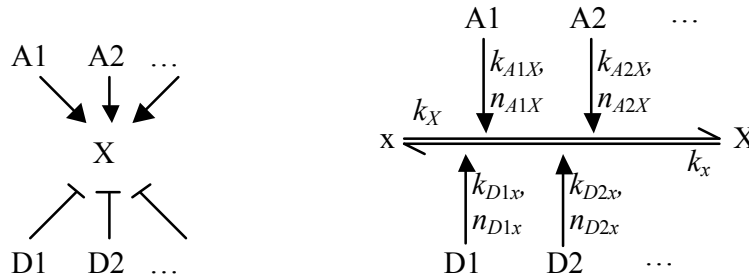
node	baseline (B)	amplitude (A)	EC_{50} (E)	Hill coop. (N)
GPCR	0	1	5	1
G-protein	0.047	0.953	4.95	1.5
Fus3	0.12	0.39	0.62	0.76
PRM1	0.047	0.953	2.67	1.24

2. Modeling scheme

2.1. Steady-state node activities as functions of their inputs

This section describes the mathematics that we used to compute steady-state node activities for cases where arrows affected the activity levels of nodes. The following section addresses arrows that affect other arrows. We present these mathematics in a general fashion in part because this enables its application to all of the network topologies that we explored, but also because a general approach is better for revealing the structure of the equations.

Consider a node, X, which can represent any node in our model scheme. Its uncatalyzed activation and deactivation reaction rate constants are k_x and k_x , respectively. Suppose this node is also enzymatically activated by zero or more arrows that originate from nodes A1, A2, ..., and it is enzymatically deactivated by zero or more arrows that originate from nodes D1, D2, Whether these arrows arise from the active or inactive states of the source nodes does not affect this analysis. The topology and detailed diagrams for this node are



Using simple mass action kinetics, as described in the main text, the dynamics of node X are given by the differential equation

$$\frac{d[X]}{dt} = [x] \left(k_x + k_{A1X} [A1]^{n_{A1x}} + k_{A2X} [A2]^{n_{A2x}} + \dots \right) - [X] \left(k_x + k_{D1x} [D1]^{n_{D1x}} + k_{D2x} [D2]^{n_{D2x}} + \dots \right)$$

We assume that the total amount of node X is constant and set to 1, leading to the conservation equation

$$[x] + [X] = 1$$

At steady state (denoted with subscript s.s.), the above differential equation equals zero. Setting it to zero and rearranging yields the equilibrium constant for node X,

$$K_X = \frac{[X]_{s.s.}}{[x]_{s.s.}} = \frac{k_x + k_{A1X} [A1]^{n_{A1x}} + k_{A2X} [A2]^{n_{A2x}} + \dots}{k_x + k_{D1x} [D1]^{n_{D1x}} + k_{D2x} [D2]^{n_{D2x}} + \dots}$$

Combining this with the constraint that the total amount of node X equals one yields the "steady state equation," for the steady-state activity of node X,

$$\begin{aligned}
[X]_{s.s.} &= \frac{K_x}{K_x + 1} \\
&= \frac{(k_x + k_{A1X} [A1]^{n_{A1X}} + k_{A2X} [A2]^{n_{A2X}} + \dots)}{(k_x + k_{A1X} [A1]^{n_{A1X}} + k_{A2X} [A2]^{n_{A2X}} + \dots) + (k_x + k_{D1X} [D1]^{n_{D1X}} + k_{D2X} [D2]^{n_{D2X}} + \dots)}
\end{aligned}$$

This steady state equation applies to all nodes in our model scheme for cases where arrows affect nodes.

In the steady state equation, note that dividing each term in both the numerator and denominator by k_x does not affect the value of the ratio, but simply rescales all of the rate constants by $1/k_x$. It also causes the k_x term to drop out of the equation. For this reason, we typically fixed k_x to 1 and optimized all other rate constants, now with the understanding that these rate constants were measured relative to the uncatalyzed deactivation rate.

Although not essential to the computation of node steady-state activities, it is helpful to continue this analysis to investigate the functional form of the node activities as functions of their inputs. In fact, we show here that the steady state activity of node X is a Hill function of any individual input. This is unwieldy when starting with the steady state equation, so we instead start with the Hill function equation and rearrange it into the form of the steady state equation. From the main text, the Hill function is

$$H(x) = B + A \frac{x^N}{x^N + E^N}$$

This can be rearranged to the following forms:

$$H(x) = \frac{BE^N + (A+B)x^N}{E^N + x^N} \qquad H(x) = B + A - \frac{AE^N}{x^N + E^N}$$

Returning to the steady state equation, suppose that the activity of input A1, given as [A1], is the independent variable. In that case, the steady state equation can be seen to be identical to the former rearrangement of the Hill function with the following substitutions (note the notational convention that model parameters are all lower case, with the subscripts giving the arrow source and destination nodes, while the Hill function parameters are all upper case, with the subscripts giving the input and output nodes):

$$\begin{aligned}
x &= [A1] \\
B_{A1X} &= \frac{k_x + k_{A2X} [A2]^{n_{A2X}} + \dots}{k_x + k_{A2X} [A2]^{n_{A2X}} + \dots + k_x + k_{D1X} [D1]^{n_{D1X}} + k_{D2X} [D2]^{n_{D2X}} + \dots} \\
A_{A1X} &= 1 - B_{A1X} \\
N_{A1X} &= n_{A1X} \\
E_{A1X}^N &= \frac{k_x + k_{A2X} [A2]^{n_{A2X}} + \dots + k_x + k_{D1X} [D1]^{n_{D1X}} + k_{D2X} [D2]^{n_{D2X}} + \dots}{k_{A1X}}
\end{aligned}$$

In words, the steady state equation is a Hill function of [A1] and these are the parameters for this Hill function. This is true for all values of the other inputs. Analogous results apply to all other activating inputs, such as A2. Next, suppose that the activity of D1, given as [D1], is the

independent variable. In that case, the steady state equation can be seen to be identical to the latter rearrangement of the Hill function with the following substitutions:

$$x = [D1]$$

$$B_{D1X} = \frac{k_x + k_{A1X} [A1]^{n_{A1X}} + k_{A2X} [A2]^{n_{A2X}} + \dots}{k_x + k_{A1X} [A1]^{n_{A1X}} + k_{A2X} [A2]^{n_{A2X}} + \dots + k_x + k_{D2X} [D2]^{n_{D2X}} + \dots}$$

$$A_{D1X} = -B_{D1X}$$

$$N_{D1X} = n_{D1X}$$

$$E_{D1X}^N = \frac{k_x + k_{A1X} [A1]^{n_{A1X}} + k_{A2X} [A2]^{n_{A2X}} + \dots + k_x + k_{D2X} [D2]^{n_{D2X}} + \dots}{k_{D1X}}$$

Analogous results apply to all other de-activating inputs, such as D2.

There is one exception to this finding that the steady state activity of any node is a Hill function of each individual input. It arises if there are two or more arrows from a single source to the same node, and those arrows have different reaction orders. If this happens, then the same types of simplifications performed here show the node activity is not a Hill function of that input.

The fact that node activities are nearly always Hill functions of their inputs raises the question of which Hill functions can arise through parameter variation and which cannot. As an alternate view of the same question, our modeling scheme creates a mapping between the space of model parameters and the space of Hill functions, and it is interesting to ask what the coverage is of Hill function space. This coverage represents the set of dose-response behaviors that can arise from any single node in our modeling scheme.

For the activating input A1, the equations above show that $A_{1X} + B_{1X} = 1$. This means that node X is always driven to its fully active state as the concentration of an activating input tends towards infinity. The deactivating inputs are similar. For them, the subsequent set of equations above show that $A_{1X} + B_{1X} = 0$. This means that node X is always driven to its fully inactive state as the concentration of a deactivating input tends towards infinity. These results constrain the node activity dose-response curves. Rather than having four parameters (A , B , E , and N) that can be varied through modification of the model parameters, the A and B Hill function parameters are constrained to always add to 1 for activating inputs and to 0 for deactivating inputs.

Next, it is worth noting that the Hill function baseline, amplitude, and EC_{50} value for each input to node X depend upon the concentrations of the other inputs. For this reason, it can be helpful to consider the Hill function parameters that result when only the input of interest (here, A1 or D1) has non-zero concentration. For activating inputs, the parameters for these “single-input” Hill functions are:

$$B_{A1X} = \frac{k_x}{k_x + k_{A1X}} \quad A_{A1X} = 1 - B_{A1X} \quad N_{A1X} = n_{A1X} \quad E_{A1X}^N = \frac{k_x + k_{A1X}}{k_{A1X}}$$

For the deactivating inputs, they are:

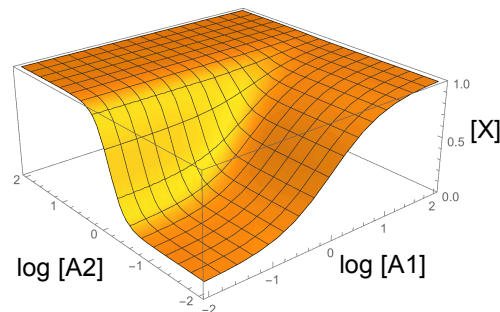
$$B_{D1X} = \frac{k_x}{k_x + k_x} \quad A_{D1X} = -B_{D1X} \quad N_{D1X} = n_{D1X} \quad E_{D1X}^N = \frac{k_x + k_x}{k_{D1X}}$$

The baseline values are the same for both the activating and deactivating inputs that are shown here, and in fact are the same for all of the inputs to node X. This value is simply the node X activity level when all inputs have zero concentration. It can be set to any value between 0 and 1, which is the entire range over which it is sensible, by modifying the k_x and/or k_x model parameters (we typically fixed k_x to 1 and varied k_x). As mentioned above, the amplitude value is fully constrained by the baseline value. The Hill coefficient value can also be set to any value in its sensible range, which is 0 to infinity, by modifying the reaction order. Finally, the EC_{50} value can be set to any value in its sensible range, which is again 0 to infinity, by modifying k_{A1X} or k_{D1X} as appropriate.

These results show the set of dose-response curves that a particular node can produce upon variation of its model parameters, where the dose represents the concentration(s) of one or more node inputs and the response is the node activity level. This is a multidimensional dose-response curve with one independent axis for each input concentration. It has the following characteristics: (i) from above, the curve is always a Hill function of each input (for inputs that do not impinge upon the same node multiple times and with different reaction orders), (ii) the baseline value, representing the condition where all inputs have zero concentration, can be made to adopt any value within its sensible range, which is from 0 to 1, by varying k_x , (iii) the amplitude for each input is constrained by the baseline value and by whether the input activates or deactivates, (iv) the Hill coefficient for each input can be made to adopt any value within its sensible range, which is 0 to infinity, and (v) the EC_{50} value for each input, provided the other inputs have zero concentration, can be made to adopt any value within its sensible range, which is 0 to infinity.

For example, suppose node X has only one input, A1. In this case, the possible dose-response curves are the set of all possible Hill functions that have a baseline between 0 and 1 and a maximum response of 1.

As another example, suppose node X has two inputs, A1 and A2. In this case, the response curve will be a function of two variables, such as that shown in the following figure.



This figure shows the baseline value as the closest point of the 3D surface, that the saturation value tends to 1 as either input is made large, and that the response is a Hill function along (or parallel to) any of the gridlines shown in the figure. In particular, the response is a Hill function on the two close faces of this 3D figure; these single-input Hill functions represent the response where one input is varied and the other is fixed at essentially 0 concentration. In this 2-input

case, the model parameters can be adjusted to give any baseline value, any EC_{50} for either of the single-input Hill functions, and any Hill coefficient for either input.

2.2. Two-input control reactions (two-input arrows)

Some topologies, including T14 to T19, included arrows that acted on other arrows. We called these “secondary” arrows, which acted on “primary” arrows. In our typical procedure for computing their influence, we first replaced secondary arrows that had negative influences (i.e. end with T-bar arrowhead) with ones that arose from the opposite state of the origin node and had positive influences. For example, the lower diagram for topology T15 in Figure 3 shows a negative feedback; we replaced it with a low-true positive feedback, as shown in the upper diagram. Next, we computed the influence of the two positive arrows by multiplying the activity values at their origins. In topology T15, this implies that the differential equation for node B is

$$\frac{d[B]}{dt} = \left(k_B + k_{AB} [A]^{n_{AB}} + k_{AbB} [A]^{n_{AbB1}} [b]^{n_{AbB2}} \right) [b] - k_b [B]$$

Within the parentheses, the first term represents the uncatalyzed activation rate, the second term represents the simple arrow from node A to node B, and the third term represents the second arrow from node A to node B, which is influenced by a low-true positive feedback from node B. This method expands trivially to 3-input and higher multi-input arrows. To return to the negative feedback interpretation of this topology, we used the conservation equation for node B to rewrite this equation as

$$\frac{d[B]}{dt} = \left(k_B + k_{AB} [A]^{n_{AB}} + k_{AbB} [A]^{n_{AbB1}} (1 - [B])^{n_{AbB2}} \right) [b] - k_b [B]$$

Focusing on the third term within parentheses, this represents linear inhibition, in which node B inhibits its own activation in direct proportion to its own activity. The other topologies in which arrows acted on other arrows were analogous.

For topology T15, we also investigated hyperbolic inhibition, defining the node B kinetic equation as (we only investigated the case of first order reaction rates),

$$\frac{d[B]}{dt} = \left(k_B + k_{AB} [A] + \frac{k_{AbB1} [A]}{1 + k_{AbB2} [B]} \right) [b] - k_b [B]$$

Here, node B inhibits its own activation according to Michaelis-Menten kinetics, which are likely to be more biochemically reasonable than linear inhibition. However, neither negative feedback mechanism enabled better DoRA than the simple linear topology. The reason was that the negative feedbacks decreased node B responses at high input values, which were precisely the values where node B needed greater activity to fit the target dose-response curves. We did not investigate the other topologies using this hyperbolic inhibition approach.

2.3. Justification for our modeling scheme

The biological relevance of our results relies on the biological validity of our modeling scheme. Mechanistic models (e.g. (Kofahl and Klipp, 2004)) have a direct correspondence between model and biological details, providing a means to assess one aspect of whether their

conclusions are likely to reflect biological reality or not. Our modeling scheme, by contrast, is abstract. In particular, the biochemical reactions within our nodes often do not correspond directly to those of specific individual reactions and single steps within our models may represent multiple biochemical events. Two arguments support our development and use of this scheme.

First, any model that is expressed in our modeling scheme can be constructed using real biochemical reactions, at least in principle. As explained in the discussion of Michaelis-Menten reactions in the main text, one would build such a reaction network using enzymatic reactions in which each enzyme operates in the limit of low saturation. Because of this, all of our results in which we say that a model topology can do something (e.g. a push-pull mechanism can produce DoRA) are strong. In other words, results from models using our scheme show that a biochemical reaction network could be engineered that corresponded closely to those specific models, and would produce the same behavior(s).

However, our modeling scheme cannot represent all types of biochemical reactions. As just one example, our scheme assumes that the total concentration of each species remains constant but that these species simply interconvert between inactive and active states. This two state model is clearly a substantial simplification for many real biochemical systems. For this reason, all of our results in which we say that no model built in our scheme can produce some behavior (e.g. there is no model in our scheme in which negative feedback can produce DoRA) are weak. In other words, there may be biochemical mechanisms that can produce the stated behavior but that cannot be represented in our modeling scheme.

For these negative results, we turn to the second justification. It is that each node's steady-state activity level in our modeling scheme, regardless of the model topology, is a Hill function of each of its inputs (section 2.1) *and* the dose-response behaviors observed in many biological systems are also described well by Hill functions. For example, Hill functions can be used to represent receptor-ligand binding (Clark, 1926, 1933), enzymatic catalysis (Goldbeter and Koshland, 1981), enzymatic catalysis over sequential steps (Black and Leff, 1983), and enzymatic catalysis over sequential steps with multisite phosphorylation (Huang and Ferrell, 1996). They are also observed in experimental dose-response curves, including in oxygen-hemoglobin binding (Hill, 1910), drug interactions on muscles (Clark, 1933) and receptors (Goutelle et al., 2008), and in the yeast data that we investigated in this work (section 1). That is, the functional dependencies in our modeling scheme generally agree well with those in biological systems. Furthermore, by modifying arrow rate constants and other model parameters, one can arrange that the node steady-state activity levels can be essentially any physiologically sensible Hill function of the input node (section 2.1). Thus, the functional dependencies in our modeling scheme have the same quantitative range as those in biological systems. As a result, if a biological system exhibits some specific dose-response relationship, that relationship can probably be described by Hill functions, and, if so, it can be modeled using our scheme. Or, turning this around, if models built in our scheme cannot exhibit some behavior, then biological systems with similar network topologies probably cannot either. This is a less strong statement than our first justification enabled, and it makes our negative results suggestive but not conclusive. For example, our result that systems with linear topologies cannot produce DoRA is true for biological systems that have Hill function dose-response relationships, but does not necessarily hold for those that don't.

These ideas can also be understood by considering spaces of dose-response behaviors. Our modeling scheme (nearly always) produces dose-response behaviors that are Hill functions

and that obey the constraints listed above in section 2.1. This is the dose-response space of our modeling scheme. Biological systems can, at least in principle, produce all of the same dose-response behaviors and many more as well. This means that our model dose-response space lies strictly within subset of biological dose-response space.

3. Model optimization and analysis

3.1. The SWRMS fit distance metric

To optimize the parameter values of a given model, we needed a metric with which we could quantify the difference between model and target dose-response curves. Most importantly, this metric needed to accurately reflect the qualitative concept of dose-response alignment. This led to our identification of the four following criteria that we decided that a our metric needed to exhibit. (i) The metric should return a value of 0 when the curves are identical and larger values for increasing differences between curves. (ii) The metric should be sensitive to differences in curve EC_{50} values, steepnesses (Hill coefficients), baselines, and amplitudes. The EC_{50} and steepness values are clearly important because they determine the curve shape. We also decided to include baselines and amplitudes because these are typically well-defined physical properties and models that can fit all physical properties are generally better representations of reality than those that can fit only a few of them. Also, as the main text describes, ignoring the baseline and amplitude parameters enables some models to nominally exhibit DoRA but have zero amplitude, making them biologically unrealistic. (iii) The metric should return finite values even when the curves have different baselines or amplitudes. This criterion is important because it enables the metric to be sensitive to all curve differences simultaneously. Standard unweighted least squares approaches do not obey this criterion. (iv) The metric should be invariant to input value units and to whether input values are plotted on linear or logarithmic scales. This criterion is important because the concept of dose-response alignment is not tied to a specific way of graphing dose-response curves. Standard unweighted least squares approaches do not obey this criterion either.

Based on these criteria, we developed the Slope-Weighted Root Mean Square (SWRMS) distance. From the main text, we defined it the SWRMS fit distance between model and target dose-response curves, $y_m(I)$ and $y_t(I)$ respectively, with the equation

$$d = 100 \sqrt{\int_0^{\infty} [y_m(I) - y_t(I)]^2 \left[c_t \left| \frac{dy_t(I)}{dI} \right| + c_m \left| \frac{dy_m(I)}{dI} \right| \right] dI}$$

where

$$c_t = \frac{1}{2|y_t(\infty) - y_t(0)|} \quad c_m = \frac{1}{2|y_m(\infty) - y_m(0)|}$$

The initial factor of 100 expresses the total fit distance, d , as the percentage of the worst possible fit. Perfect agreement between two dose-response curves results in a distance of 0, whereas complete disagreement (e.g. in the limit of $y_m \rightarrow 0$ and $y_t \rightarrow 1$, for all I) results in a distance of 100. The c_t and c_m parameters equalize the weighting on the two dose-response curves using their ranges.

In essence, this metric is a simple weighted sum of squared errors, very much like the standard χ^2 and “residual sum of squares” statistics (Larsen and Marx, 2012; Press et al., 1988). For reference, χ^2 is conventionally defined as

$$\chi^2 = \sum_{i=1}^n \left(\frac{m_i - x_i}{\sigma_i} \right)^2$$

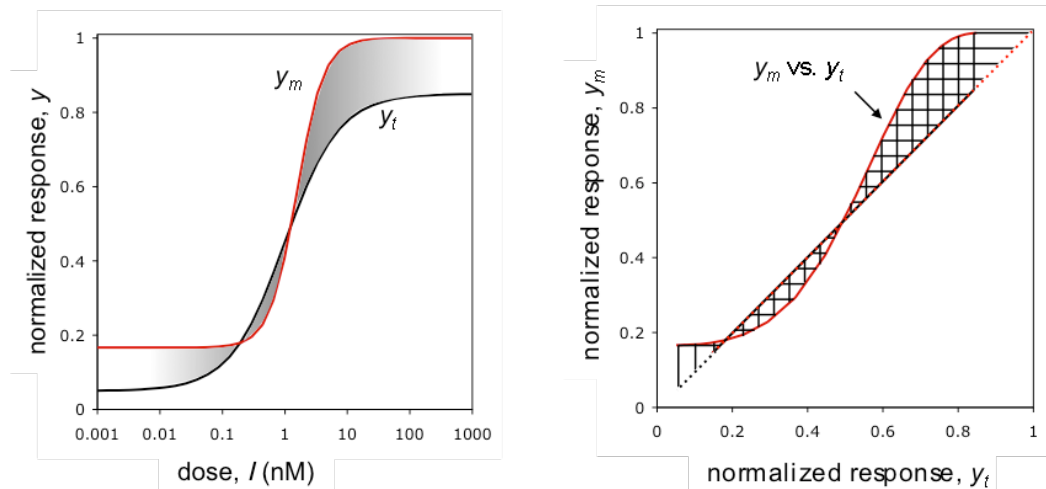
where x_i values are a set of experimental observations, m_i values are model values, σ_i values are experiment standard deviations, and there are n total observations. When used as a goodness-of-fit metric, the model is typically varied so as to minimize the differences between m_i and x_i , weighted by σ_i . (The residual sum of squares is identical, but without the σ_i weighting factors.) The central portion of the SWRMS metric is the same weighted sum of squares. In it, the squares are $[y_m(l) - y_t(l)]^2$ and the weights are, essentially, the sums of the slopes. The absolute values of the slopes are used because the weights need to be positive, much as they are in the χ^2 equation. In most cases, the dose-response curves used in this work increased monotonically, so the absolute value computations became moot in those cases. However, some dose-response curves decreased (e.g. for T9, which includes a low-true positive feedforward), making the absolute value computations essential in those cases. In practice, we used the absolute values in all cases. Because the dose-response functions that we compared were defined continuously rather than at a finite list of discrete data points, we replaced the summation in the χ^2 equation with an integral. This integral needed to extend over the entire dose-response curves, so we set its limits from 0 to infinity. Another way of seeing why these limits are appropriate is that the weighted sum of squares needs to include the entire response ranges of both dose-response curves so that it includes all response differences, and this is only possible if the integral extends to infinity. The dose-response slopes tend to zero as the l value tends towards infinity, causing this portion of the integral to have a minimal influence (this is criterion *iii*, above).

In practice, we used the SWRMS metric as expressed above. However, a different arrangement helps elucidate its properties. For the typical case that both dose-response curves increase monotonically, the metric rearranges to

$$d = 100 \sqrt{c_t \int_{y_t(0)}^{y_t(\infty)} (y_m - y_t)^2 dy_t + c_m \int_{y_m(0)}^{y_m(\infty)} (y_m - y_t)^2 dy_m}$$

Notably, the input value, l , does not appear in this equation. This fact reflects the metric's independence to the input units and also whether the input is graphed on a linear or logarithmic scale (criterion *iv*, above).

The two SWRMS equations can be understood with reference to the following figure. The panel on the left shows model and target dose-response curves as functions of the input value. The SWRMS metric can be computed with the first equation by integrating the difference between the two curves, while weighting this difference using, approximately, the sum of the curve slopes, which the shading depicts. The panel on the right shows a parametric plot of y_m as a function of y_t in red. The diagonal line represents the case $y_m = y_t$, so deviations from this diagonal represent differences between the two dose-response curves. The SWRMS metric is computed here using the second equation, now with one integral summing the squared vertical deviations and the other integral summing the squared horizontal deviations (the straight lines show the integral slices). The overall deviation of the parametric curve from the main diagonal is a good qualitative measure of the goodness of fit, and one that corresponds closely to the SWRMS distance.



Although it is reasonably unimportant to its use as a fitting metric, it is interesting to note that the SWRMS distance obeys three of the four properties required of a metric for a mathematical metric space. The properties are: (i) non-negativity, meaning that $d(x,y) \geq 0$, (ii) identity of indiscernibles, meaning that $d(x,y) = 0$ if and only if $x = y$, (iii) symmetry, meaning that $d(x,y) = d(y,x)$, and (iv) triangle inequality, meaning that $d(x,y) + d(y,z) \geq d(x,z)$. It is straightforward to show that the SWRMS distance obeys the first three properties. However, by trial and error, we found that it can fail the triangle inequality. Our example that failed was based on three Hill functions, each with baseline 0 and Hill coefficient 1: amplitudes and EC_{50} s for the three Hill functions were 1 and 1 for Hill function x , 0.5 and 1 for Hill function y , and 0.5 and 10 for Hill function z , respectively. Using these numbers, we found that the SWRMS distances were 28.8 between x and y , 18.2 between y and z , and 52.8 between x and z . The sum of the first two distances is less than the third by 5.7, thus showing the failure of the triangle inequality.

Every model produced a separate dose-response curve for each node, each of which was compared to the appropriate target function. We computed the SWRMS distance for the entire model as the arithmetic mean of the SWRMS distances for the individual dose-response curves away from their specific target functions.

A potential concern with our use of the SWRMS distance is that it may place an excessive importance on dose-response curve amplitudes as opposed to their EC_{50} s, which might be more biologically significant. We addressed this issue in several ways. First, we used a different metric in preliminary work that quantified dose-response curve differences by fitting Hill functions to the model data and then comparing those Hill function parameters to the Hill function parameters of the target curves. Even when we weighted this metric to strongly emphasize EC_{50} 's, rather than amplitude differences, we found the same qualitative results as are described in the main text. Second, changing the dose-response targets from the 4-node idealized targets, in which all dose-response amplitudes equaled one, to the yeast PRS targets, in which one amplitude was much less than one (thus making it easier to fit), still showed the same qualitative results. Finally, we also investigated several other sets of yeast PRS targets that had lower amplitudes for the Prm1 and/or G-protein nodes (A_{PRM1} was 0.35 and A_{Gprt} was 0.8) which again made the amplitudes easier to fit but did not affect qualitative results. Thus,

the precise fit distances and the optimal model parameters clearly depend on the fit metric definition, but the qualitative results of this work do not.

Another possible concern with our use of the SWRMS distance is that it is removed from the quantity that is actually of interest, which is information transmission through the signaling system. We chose the SWRMS distance because the information transmission cannot be computed without making assumptions about the noise within the signaling system. (In the absence of noise, essentially all possible combinations of dose-response curves transmit information completely perfectly, making that assumption not informative.) We do not have adequate experimental data to estimate the noise levels for the yeast data, so we decided to avoid making assumptions about the noise throughout this work. Nevertheless, this raises the interesting open question about how well the SWRMS distance correlates with information transmission.

3.2. The DoRA-score, used in preliminary work

Before developing the SWRMS distance metric, we quantified the difference between model and target dose-response curves using a different metric, a “DoRA-score.” To use it, we fit model dose-response curves with Hill functions and then compared the differences between model and target Hill function parameters. The equation is

$$d = \sqrt{\sum_{i \in \text{nodes}} \sum_{j \in \{B,A,E,N\}} w_{i,j} (\text{model}_{i,j} - \text{target}_{i,j})^2}$$

where i is an index that scans over the nodes in a model, j is an index for the Hill function parameter (B for baseline, A for amplitude, E for EC_{50} , and N for Hill cooperativity), $w_{i,j}$ is a matrix of weighting factors, $\text{model}_{i,j}$ is the j 'th Hill parameter for the model dose-response curve for the i 'th node, and $\text{target}_{i,j}$ is the j 'th Hill parameter for the target dose-response curve for the i 'th node. This metric obeyed the four criteria that we considered essential, listed above in section 3.1. However, it also had the problems of being arbitrary and not working well when dose-response curves weren't Hill functions. In addition, it was not clear how the weights should be chosen. For these reasons, we replaced it with the SWRMS distance.

Notably, we found the same qualitative results with this DoRA-score as we found later with the SWRMS distance. In particular, using this DoRA-score, we found that linear topologies and those with most feedbacks and feedforwards could not produce good DoRA. We also found that fits were substantially better when we allowed model reactions to be cooperative rather than constraining them to be non-cooperative. In addition, we found that the models with push-pull mechanisms could exhibit DoRA. Furthermore, these qualitative results did not change when we varied the DoRA-score weighting factors; we typically set all of them to 1, but also explored other options, including setting multiple values to 0.

The qualitative similarity between the results that we found with the SWRMS distance and those with the DoRA-score suggests that the conclusions of this work arose from genuine differences between models, rather than artifacts of the SWRMS distance.

3.3. Optimization methods

We optimized model parameters using a combination of greedy random walk and downhill simplex methods (Press et al., 1988), both of which are types of stochastic optimization (Moles et al., 2003; Schneider and Kirkpatrick, 2006). In both cases, our NodeSolver software started the optimization with user-defined model parameters (or, sometimes, random parameters) and then iteratively improved them until SWRMS fit distances stopped decreasing. We deemed a solution optimal only when we found it repeatedly from many different starting values.

In our greedy random walk method, NodeSolver software computed the SWRMS distance for a model with an initial set of parameters. It then took a trial step in parameter space by changing one randomly chosen parameter by a random displacement (chosen from a Gaussian distribution with a standard deviation of 1 initially) and computed the SWRMS distance for the modified model. If this trial step reduced the SWRMS distance, the modification was kept and the standard deviation for that parameter was increased by 20%. Otherwise, the trial step was rejected, returning the model to its prior parameters, and the standard deviation for that parameter was reduced by 1%. NodeSolver repeated this procedure about 10,000 times for each round of fitting, which took a few seconds of computer time. This procedure was slow but very robust, meaning that it always led to local minima.

Our downhill simplex method closely followed the procedure described in *Numerical Recipes in C* (Press et al., 1988). In brief, the algorithm defines a high-dimensional triangle which has as many vertices as there are fitting parameters, which is called a simplex, and then propagates this simplex through parameter space to the optimal location. NodeSolver performed about 10,000 propagation steps for each round of fitting. This procedure was fast but our implementation of it did not always work reliably when models were complicated or parameters were highly correlated.

Simple models, such as the two-node models with non-cooperative reactions and only one control arrow, generally required ten or fewer rounds of fitting with no user input. Complicated models, such as ones with all possible control arrows, ones with non-linear reaction orders, and those with the yeast experimental data, sometimes required fifty or more rounds of fitting with intermittent input from us. This input would typically entail fixing model parameters that appeared to be fully optimized so that more computation would be directed towards the other parameters, setting bounds on the parameter search ranges to avoid local minima, adjusting parameters to get the current search location away from a local minimum (typically evidenced by model dose-response curves having zero amplitude), and changing the list of fittable parameters to ones that seemed more likely to lead to success (e.g. for a two-node model, we typically fixed k_b to 1 because it is redundant with other parameters, but sometimes we got better fitting results when this was made a fittable parameter). This user input adds bias to the fitting procedure, but we believe that all of our reported results represent the global minima based on the fact that we found them multiple times from multiple different starting points.

We also tried to minimize SWRMS distances using simulated annealing (Schneider and Kirkpatrick, 2006) and greedy random walk methods that varied multiple parameters with each step. Those methods did not prove to be as useful as the above-mentioned ones, at least with our implementations of them, and did not figure in the results in this manuscript.

3.4. Akaike Information Criterion computation

To determine whether the roughly 3-fold improvements from increasing steepness were significant rather than a consequence of adding additional fitting parameters, we computed Akaike Information Criterion (AIC) values for each model (Document S1). It is an assertion generally acknowledged that models with lower AIC values, which can arise through better fits and/or fewer model parameters, represent the data better (Burnham and Anderson, 2002). Here, we found that enabling changes in reaction order always decreased AIC values, with an average decrease of 17.6 units. By contrast, adding control arrows, which also added fitting parameters, typically increased AIC values. Both results argue that models that allowed different reaction orders represented the target functions better than those that did not.

The Akaike Information Criterion (AIC) is a measure of the ability of models to fit data, thereby providing a means for selecting between multiple candidate models. The AIC value is given with the equation (Burnham and Anderson, 2002)

$$AIC = -2 \ln L + 2K$$

where K is the number of model parameters and L is the likelihood of the model. The likelihood is the probability that the observed data could have arisen, given the model. Models with smaller AIC values are better than those with higher AIC values, where in this case better means that there is less information loss in representing the data with the model (see (Burnham and Anderson, 2002)). The $-2 \ln L$ term in the AIC equation rewards models that fit the data well while the $2K$ term penalizes those that use more parameters to do so. Thus, the AIC value represents a balance between quality of fit and model parsimony (few parameters).

The AIC is not particularly practical in this general form. To calculate it here, we began with the fact that it is conventional to assume that the data include independent normally distributed errors with constant variance (Burnham and Anderson, 2002). With this assumption, the AIC becomes

$$AIC = n \ln(s^2) + 2K + C$$

where n is the number of data points, s^2 is the estimated variance, and C is a constant. The actual value of C is ignored here because only the differences between AIC values are relevant. Note that the value of K is the total number of estimated model parameters, including the variance. The value of s^2 is the mean sum of squared errors (Burnham and Anderson, 2002),

$$s^2 = \frac{1}{n} \sum_{i=1}^n (m_i - x_i)^2$$

where m_i and x_i are the model and data values at point i , as in section 3.1. This s^2 value is very close to the χ^2 value introduced above, which was

$$\chi^2 = \sum_{i=1}^n \left(\frac{m_i - x_i}{\sigma_i} \right)^2$$

Thus, we rewrote the AIC equation for χ^2 ,

$$AIC = n \ln(\chi^2/n) + 2K + C$$

Additional constant terms got subsumed into C here. This change relieved the assumption that the variance is constant for all data points because the χ^2 statistic allows for a different variance

at each data point. The squared SWRMS distance, d^2 , is a weighted sum of squares, just like χ^2 . This means that the AIC can also be written as

$$AIC = n \ln(d^2/n) + 2K + C$$

Yet more terms got subsumed into C . A problem arises at this point. Our computation of the SWRMS is performed with an integral over an infinite number of “data points”, rather than the sum that is used for the χ^2 statistic. However, taking the limit of n going to infinity in the above equation increases the AIC to infinity. More importantly though, it shifts all of the emphasis in the AIC towards the quality of the fit and away from the number of fit parameters, thereby negating the entire purpose of using the AIC. On a deeper level, the problem with taking n to infinity is that the AIC derivation assumed that the n data points have independent errors, whereas adjacent points in noise-free dose-response curves, as used here, are clearly not independent. This raises the question of how many independent points are represented by a single noise-free dose-response curve. We concluded that there are 4 points because all of the dose-response curves in this work are 4-parameter Hill functions; alternatively, any 4 points in a dose-response graph are sufficient to uniquely determine the parameters of the 4-parameter Hill function that includes them. Based on these arguments, we computed AIC values using the equation

$$AIC = 4T \ln\left(\frac{d^2}{4T}\right) + 2K$$

where T is the number of nodes that are fit to target functions.

For example, consider the 2-node linear topology, T1. Using non-cooperative reactions, its SWRMS distance was 5.55, so d^2 was 30.8. The fit included 5 unknown parameters, k_A , k_{IA} , k_B , k_{AB} , and the SWRMS distance, so K was 5. We fit both nodes A and B to target functions (which happened to be identical to each other), so T was 2. From these values the AIC was 20.8. Using the same linear topology but with cooperative reactions, its SWRMS distance was 1.86 and the number of unknown parameters increased by 2 to 7. Its AIC was 7.3. This large AIC decrease shows that including cooperativity leads to a qualitatively better model.

From differences in AIC values, it is possible to compute the likelihood that one model reduces the information loss when compared to another model, which is called the relative likelihood or evidence ratio (Burnham and Anderson, 2002). It is

$$L_r = \exp\left(-\frac{\Delta AIC}{2}\right)$$

where ΔAIC is the AIC difference between two models. Continuing with the above example, $\exp(-(20.8-7.3)/2) = 0.001$. This suggests that the linear topology with cooperativity is 1000-fold more likely to minimize the information loss from the target functions than the linear topology without cooperativity. The precise meaning of this result is unclear because the target functions are continuous noise-free curves rather than discrete data points with independent additive Gaussian-distributed noise, as is assumed for the AIC. Nevertheless, it does show that the difference between 20.8 and 7.3 is quite large.

3.5. Robustness computation

We tested each optimized model for robustness to parameter variation. When a model is optimized, this means that its SWRMS distance value is the minimum possible value and that the SWRMS distance will increase if parameters are moved away from this optimum position in parameter space. To test robustness, we varied the parameters to random values that were up to 3-fold away from their optimum values (see below) to produce a trial model, and then computed the SWRMS distance for the trial model. We repeated this 10^5 times and counted the number of the trial models for which the SWRMS value was (i) less than 3 SWRMS units above the distance for the optimal model and (ii) less than 3 SWRMS units above 0. In both cases, we divided the result by 10^3 to yield the percent of trials that were below the respective SWRMS threshold. We called the first result, in which the threshold is relative to the optimal SWRMS distance, the relative robustness. It tested the robustness of the optimal model to parameter variation. That is, for a topology that has already been optimized, this tests how well it will exhibit DoRA if the parameters move a short distance away from their optimal values. We called the second result, in which the threshold is 3 units above an SWRMS distance of 0, the absolute robustness. It tested the likelihood of achieving partial DoRA (*i.e.* $d < 3$) with a given topology when searching parameter space randomly. This absolute robustness value is comparable to the “Q-value” used by Yan et al. (Yan et al., 2012).

To explain our parameter variation method, consider a vector of optimized parameters $\{k_1, k_2, k_3, \dots, k_n\}$, where there are n total parameters. The obvious way to vary the parameters by up to 3-fold variation is to vary each one individually, in each case picking a uniformly distributed random number between $1/3$ and 3 times the optimal value. For example, k_1 would be replaced by a uniformly distributed random number between $k_1/3$ and $3k_1$, the same procedure would apply to k_2 , and so forth. The problem with this method is that the results are highly dependent on dimensionality. If there is one parameter, for example, the maximum possible variation away from the origin is $3k_1$. However, if there are two parameters, then the maximum possible variation away from the origin is $\{3k_1, 3k_2\}$, which is, in some sense, farther away from the optimum than just $3k_1$. This problem gets worse with higher dimension because it becomes increasingly likely for random points to be near one or more of the edges of the parameter variation domain. The solution is not to pick each parameter’s variation independently but to pick them so that the total variation is uniformly distributed with a 3-fold variation maximum.

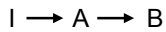
This is easiest to consider using the logarithms of the parameters, so the optimum becomes $\log \mathbf{k} = \{\log k_1, \log k_2, \log k_3, \dots, \log k_n\}$. Three-fold variation is now represented by adding or subtracting $\log 3$. To do so, we defined an n -dimensional ball that was centered at $\log \mathbf{k}$ and had radius $\log 3$. We picked random variables uniformly within the volume of this ball as the trial parameters. Inverting the logs by exponentiating the values led to the parameters that we entered into the model. This approach keeps a constant distribution of Euclidean distances of trial parameters about the optimal parameters, independent of the number of parameters. In essence, this samples from an n -dimensional sphere of parameter space rather than an n -dimensional cube.

4. Results for two-node topologies

4.1 Two-node topologies with single control arrows

This section presents the optimized parameters for each two-node topology. It presents them for models that were constrained to use only non-cooperative reactions and for models that could include cooperative reactions as well, meaning that we optimized the reaction orders too. For some topologies, this section also presents additional analytical or simulation results. In each data table, asterisks next to parameters indicate that the parameter was included in the fitting, while parameters without asterisks were constrained to the value shown.

T1 - linear topology



parameter	non-coop.	cooperative
k_A	0*	0*
k_a	1	1
k_{IA}	1*	1*
n_{IA}	1	1*
k_B	0*	0.134*
k_b	1	1
k_{AB}	2.234*	6.709*
n_{AB}	1	2.797*
node A SWRMS	0	0
node B SWRMS	11.09	3.72
overall SWRMS	5.546	1.862
AIC	20.77	7.31
rel. robustness	133	20
abs. robustness	0	0.9

Differential equations and steady-state node activities:

$$[\dot{A}] = [a](k_A + k_{IA}[I]^{n_{IA}}) - [A](k_a) \quad [\dot{B}] = [b](k_B + k_{AB}[A]^{n_{AB}}) - [B](k_b)$$

$$[A] = \frac{k_A + k_{IA}[I]^{n_{IA}}}{k_A + k_{IA}[I]^{n_{IA}} + k_a} \quad [B] = \frac{k_B + k_{AB}[A]^{n_{AB}}}{k_B + k_{AB}[A]^{n_{AB}} + k_b}$$

Substituting the optimized parameters given above (for both non-cooperative and cooperative results) into the steady-state solution for [A] yields

$$[A] = \frac{[I]}{[I] + 1}$$

This is a Hill function with zero baseline, unit amplitude, unit EC_{50} , and unit Hill cooperativity. It is identical to the target function, so the fit distance for node A is 0.

The steady-state activity for node B is a Hill function of [A], with the following Hill function parameters:

$$B_{AB} = \frac{k_B}{k_B + k_b} \quad A_{AB} = \frac{k_b}{k_B + k_b} \quad N_{AB} = n_{AB} \quad E_{AB}^{N_{AB}} = \frac{k_B + k_b}{k_{AB}}$$

We substituted the steady-state solution for [A] (using the optimized parameters) into the steady-state solution for [B] to yield the dose-response curve for [B] as a function of [I]. The solution is unwieldy (and not a Hill function) if $n_{AB} \neq 1$ but simplifies to another Hill function if $n_{AB} = 1$. In this latter case, the function and its parameters are

$$[B] = \frac{k_B + [I](k_B + k_{AB})}{k_B + k_b + [I](k_B + k_{AB} + k_b)}$$

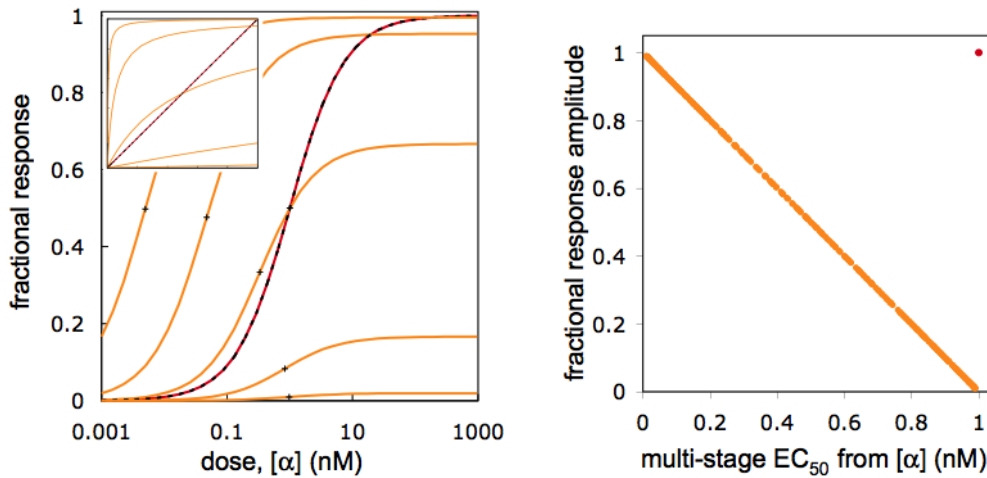
$$B_{IB} = \frac{k_B}{k_B + k_b} \quad A_{IB} = \frac{k_{AB} k_b}{(k_B + k_b)(k_{AB} + k_B + k_b)} \quad N_{IB} = 1 \quad E_{IB} = \frac{k_B + k_b}{k_{AB} + k_B + k_b}$$

For the steady-state activity of this node to agree with the target dose-response curve, B_{IB} needs to equal 0, while A_{IB} , N_{IB} , and E_{IB} all need to equal 1. The first requirement, for B_{IB} , can be achieved by setting k_B to 0, as in fact is the result of the optimal fit for first order reactions, shown above. The requirement on N_{IB} is already achieved here as well. However, the other two parameters cannot simultaneously equal their target values of 1. This becomes clearer when the $k_B = 0$ result is substituted into their equations and k_b is set to 1, which can be done without loss of generality as described in section 2.1.

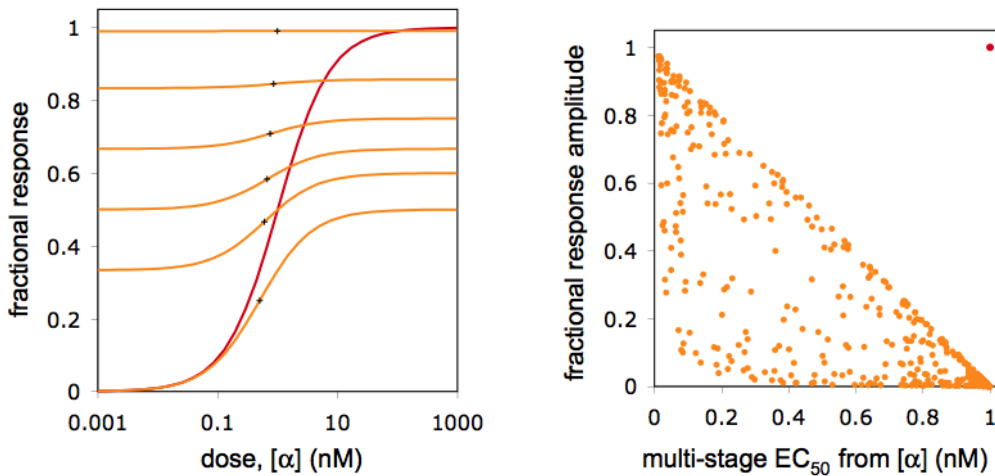
$$A_{IB} = \frac{k_{AB}}{k_{AB} + 1} \quad E_{IB} = \frac{1}{k_{AB} + 1}$$

If k_{AB} is reduced to zero, then E_{IB} equals 1, as desired, but A_{IB} equals 0. On the other hand, increasing k_{AB} towards infinity causes A_{IB} to equal 1 but then E_{IB} equals 0.

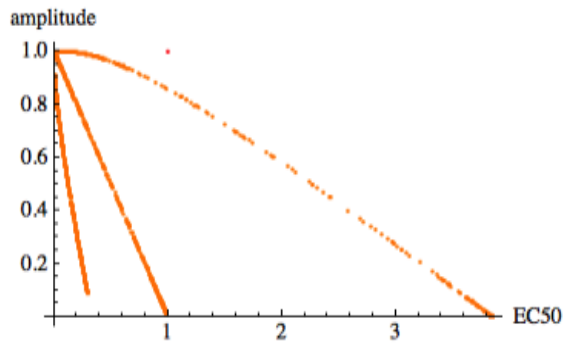
The following figures show this trade-off between a sufficiently large amplitude and a sufficiently large EC_{50} . In the left panel, the black dashed line represents the target function, the red dashed line is the dose-response function for node A ($k_a = 1$, $k_A = 0$, $k_{IA} = 1$, and $n_{IA} = 1$) and the orange lines are possible dose-response functions for node B ($k_b = 1$, $k_B = 0$, $n_{AB} = 1$, and k_{AB} differs for the curves; reading from left to right, its values are 200, 20, 2, 0.2, and 0.02, respectively). '+' symbols in the figure depict the half-maximum points, which give the EC_{50} values. The inset shows a parametric plot of the node B response as a function of the node A response, where the diagonal line represents perfect alignment. The right panel graphs the node A and B Hill function amplitudes on the y-axis against their EC_{50} values on the x-axis. The red point represents the Hill function parameters for node A, which is the same as those for the target function. The orange points represent the node B parameters for 500 different k_{AB} values, chosen randomly between 0.01 and 100. For the system to exhibit DoRA, it would have to be possible for an orange dot to be at the location of the red dot, which clearly does not happen.



The next figure illustrates the role of the k_B parameter. The red line and dot represent the dose-response function for node A, using the same parameters as before, and also represent the target dose-response function. The orange lines and dots represent node B (left panel: $k_b = 1$, $k_{AB} = 1$, $n_{AB} = 1$, and k_B values, from bottom to top, are 0, 0.5, 1, 2, 5, and 100; right panel: $k_b = 1$, $n_{AB} = 1$, and k_{AB} and k_B were randomly chosen between 0.01 and 100). These show that increasing k_B increases the node B baselines and decreases the node B amplitudes but do not improve the ability of node B to equal the target function.

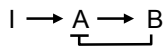


The next figure illustrates the role of the reaction order, n_{AB} , showing how increasing it enables a better fit to the target function. The red point represents the dose-response of node A using the same parameters as before, which is also the target function. The orange points represent dose-responses of node B, each for 500 randomly chosen k_{AB} values between 0.01 to 100. The n_{AB} values for these lines are 0.5 for the left line, 1 for the middle line (identical to ones above), and 3 for the right line (also, $k_b = 1$ and $k_B = 0$).



This figure shows that increasing the reaction order of the arrow from A to B simultaneously increases the amplitude and EC₅₀ for the node B dose-response curve.

T2 - negative feedback



parameter	non-coop. control fixed	non-coop. control fit	cooperative control fixed	cooperative control fit
k_A	0*	0*	0.00154*	0*
k_a	1	1	1	1
k_{IA}	1.9504*	1*	1.958*	1*
n_{IA}	1	1	1.219*	1*
k_B	0*	0*	0.125*	0.134*
k_b	1	1	1	1
k_{AB}	2.203*	2.234*	6.861*	6.709*
n_{AB}	1	1	2.769*	2.797*
k_{Ba}	2	0*	2	0*
n_{Ba}	1	1	1	1*
node A SWRMS	2.00	0	0.878	0
node B SWRMS	12.42	11.09	3.152	3.72
overall SWRMS	7.21	5.546	2.01	1.862
AIC	24.97	22.77	8.57	11.31
rel. robustness	200	132	48	46
abs. robustness	0	0	2	2

Differential equations and steady-state node activities:

$$[\dot{A}] = [a](k_A + k_{IA}[I]^{n_{IA}}) - [A](k_a + k_{Ba}[B]^{n_{Ba}}) \quad [\dot{B}] = [b](k_B + k_{AB}[A]^{n_{AB}}) - [B](k_b)$$

$$[A] = \frac{k_A + k_{IA}[I]^{n_{IA}}}{k_A + k_{IA}[I]^{n_{IA}} + k_a + k_{Ba}[B]^{n_{Ba}}} \quad [B] = \frac{k_B + k_{AB}[A]^{n_{AB}}}{k_B + k_{AB}[A]^{n_{AB}} + k_b}$$

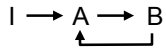
We were initially surprised that this negative feedback did not help produce DoRA. In retrospect, we realized that it did not because feedback from a downstream node to an

upstream node does not change the effect of the upstream node on the downstream node. In this particular case, the negative feedback lowers the activity of node A, but does not change the effect of A on B. Restated yet again, the steady-state activity of B is

$$[B] = \frac{k_B + k_{AB} [A]^{n_{AB}}}{k_B + k_{AB} [A]^{n_{AB}} + k_b}$$

independent of the presence of the feedback. This is the same function that arose for the linear topology (T1), with the same result, which is that [B] cannot be made to equal [A]. Yet another way of seeing this is that the negative feedback does not affect the dose-response curve of B relative to that of A, meaning that it does not affect the alignment of the two dose-response curves. This finding applied to all four types of feedbacks that originated at downstream nodes and ended at upstream nodes.

T3 - positive feedback



parameter	non-coop. control fixed	non-coop. control fit	cooperative control fixed	cooperative control fit
k_A	0*	0*	0*	0*
k_a	1	1	1	1
k_{IA}	0.696*	1*	0.154*	1*
n_{IA}	1	1	2.129*	1*
k_B	0*	0*	0.112*	0.134*
k_b	1	1	1	1
k_{AB}	0.508*	2.234*	6.325*	6.709*
n_{AB}	1	1	3.154*	2.797*
k_{BA}	2	0*	2	0*
n_{BA}	1	1	1	1*
node A SWRMS	6.45	0	5.63	0
node B SWRMS	33.16	11.09	4.45	3.72
overall SWRMS	19.81	5.546	5.04	1.862
AIC	41.14	22.77	23.24	11.31
rel. robustness	590	133	13	31
abs. robustness	0	0	0	1.5

Differential equations and steady-state node activities:

$$[\dot{A}] = [a](k_A + k_{IA} [I]^{n_{IA}} + k_{BA} [B]^{n_{BA}}) - [A](k_a) \quad [\dot{B}] = [b](k_B + k_{AB} [A]^{n_{AB}}) - [B](k_b)$$

$$[A] = \frac{k_A + k_{IA} [I]^{n_{IA}} + k_{BA} [B]^{n_{BA}}}{k_A + k_{IA} [I]^{n_{IA}} + k_{BA} [B]^{n_{BA}} + k_a}$$

$$[B] = \frac{k_B + k_{AB} [A]^{n_{AB}}}{k_B + k_{AB} [A]^{n_{AB}} + k_b}$$

Positive feedback leads to bistability in many systems, so we investigated whether it does here as well. Using equations from section 2.1 (and assuming that k_A and k_B equal 0 and that n_{IA} and n_{AB} equal 1), the node steady-state activities are

$$[A] = \frac{k_{IA}[I] + k_{BA}[B]}{k_{IA}[I] + k_{BA}[B] + k_a} \quad [B] = \frac{k_{AB}[A]}{k_{AB}[A] + k_b}$$

Substituting the latter equation into the former leads to

$$[A] = \frac{(k_{IA}k_{AB}[I] + k_{AB}k_{BA})[A] + k_{IA}k_b[I]}{(k_{IA}k_{AB}[I] + k_{AB}k_{BA})[A] + k_{IA}k_b[I] + k_a}$$

For notational convenience, define

$$c_1 = k_{IA}k_{AB}[I] + k_{AB}k_{BA} \quad c_2 = k_{IA}k_b[I]$$

These simplify the prior equation to

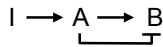
$$[A] = \frac{c_1[A] + c_2}{c_1[A] + c_2 + k_a}$$

Solving for [A] yields

$$[A] = \frac{-(c_2 - c_1 + k_a) \pm \sqrt{4c_1c_2 + (c_2 - c_1 + k_a)^2}}{2c_1}$$

This solution is only sensible when [A] is a non-negative number. If c_1 and c_2 are greater than zero, then taking the negative option for the \pm symbol always yields a negative value for [A] because the square root term is always larger than the absolute value of $(c_2 - c_1 + k_a)$. Thus, only the positive option is sensible. The positive option can be seen to yield non-negative values for [A] for any c_1 , c_2 , and k_a values, meaning that there is a single solution when c_1 and c_2 are greater than zero. From its definition, c_1 cannot equal zero. However, if c_2 equals zero (only possible when k_b , k_{IA} , or [I] equal zero), then the solution is bistable with solutions $[A] = 0$ and $[A] > 0$.

T4 - negative feedforward



parameter	non-coop. control fixed	non-coop. control fit	cooperative control fixed	cooperative control fit
k_A	0*	0*	0*	0*
k_a	1	1	1	1
k_{IA}	1*	1*	1*	1*
n_{IA}	1	1	1*	1*
k_B	0*	0*	0.142*	0.134*
k_b	1	1	1	1
k_{AB}	3.972*	2.234*	18.221*	6.709*
n_{AB}	1	1	3.091*	2.797*
k_{Ab}	2	0*	2	0*

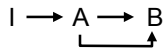
n_{Ab}	1	1	1	1*
node A SWRMS	0	0	0	0
node B SWRMS	15.94	11.09	4.22	3.72
overall SWRMS	7.97	5.546	2.11	1.862
AIC	26.57	22.77	9.29	11.31
rel. robustness	158	132	19	32
abs. robustness	0	0	0.3	1.5

Differential equations and steady-state node activities:

$$[\dot{A}] = [a](k_A + k_{IA}[I]^{n_{IA}}) - [A](k_a) \quad [\dot{B}] = [b](k_B + k_{AB}[A]^{n_{AB}}) - [B](k_b + k_{Ab}[A]^{n_{Ab}})$$

$$[A] = \frac{k_A + k_{IA}[I]^{n_{IA}}}{k_A + k_{IA}[I]^{n_{IA}} + k_a} \quad [B] = \frac{k_B + k_{AB}[A]^{n_{AB}}}{k_B + k_{AB}[A]^{n_{AB}} + k_b + k_{Ab}[A]^{n_{Ab}}}$$

T5 - positive feedforward

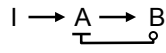


parameter	non-coop. control fixed	non-coop. control fit	cooperative control fixed	cooperative control fit
k_A	0*	0*	0*	0*
k_a	1	1	1	1
k_{IA}	1*	1*	1*	1*
n_{IA}	1	1	1*	1*
k_B	0*	0*	0*	0.0381*
k_b	1	1	1	1
k_{AB}	0.234*	2.234*	19.331*	17.491*
n_{AB}	1	1	8.76*	9.326*
k_{AB2}	2	0*	2	2.948*
n_{AB2}	1	1	1	1.659*
node A SWRMS	0	0	0	0
node B SWRMS	11.09	11.09	4.63	0.839
overall SWRMS	5.546	5.546	2.31	0.42
AIC	20.77	22.77	10.78	-12.53
rel. robustness	343	132	95	17
abs. robustness	0	0	5	9

Differential equations and steady-state node activities:

$$[\dot{A}] = [a](k_A + k_{IA}[I]^{n_{IA}}) - [A](k_a) \quad [\dot{B}] = [b](k_B + k_{AB}[A]^{n_{AB}} + k_{AB2}[A]^{n_{AB2}}) - [B](k_b)$$

$$[A] = \frac{k_A + k_{IA}[I]^{n_{IA}}}{k_A + k_{IA}[I]^{n_{IA}} + k_a} \quad [B] = \frac{k_B + k_{AB}[A]^{n_{AB}} + k_{AB2}[A]^{n_{AB2}}}{k_B + k_{AB}[A]^{n_{AB}} + k_b}$$

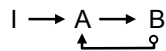
T6 - low-true negative feedback

parameter	non-coop. control fixed	non-coop. control fit	cooperative control fixed	cooperative control fit
k_A	0.0281*	0*	0*	0*
k_a	1	1	1	1
k_{IA}	1.88*	1*	1.944*	1*
n_{IA}	1	1	0.779*	1*
k_B	0*	0*	0.122*	0.134*
k_b	1	1	1	1
k_{AB}	2.314*	2.234*	6.001*	6.709*
n_{AB}	1	1	2.585*	2.797*
k_{ba}	2	0*	2	0*
n_{ba}	1	1	1	1*
node A SWRMS	1.76	0	0.884	0
node B SWRMS	9.96	11.09	4.19	3.72
overall SWRMS	5.86	5.546	2.535	1.862
AIC	21.65	22.77	12.25	11.31
rel. robustness	234	134	26	32
abs. robustness	0	0	0.2	1.5

Differential equations and steady-state node activities:

$$[\dot{A}] = [a](k_A + k_{IA}[I]^{n_{IA}}) - [A](k_a + k_{ba}[b]^{n_{ba}}) \quad [\dot{B}] = [b](k_B + k_{AB}[A]^{n_{AB}}) - [B](k_b)$$

$$[A] = \frac{k_A + k_{IA}[I]^{n_{IA}}}{k_A + k_{IA}[I]^{n_{IA}} + k_a + k_{ba}[b]^{n_{ba}}} \quad [B] = \frac{k_B + k_{AB}[A]^{n_{AB}}}{k_B + k_{AB}[A]^{n_{AB}} + k_b}$$

T7 - low-true positive feedback

parameter	non-coop. control fixed	non-coop. control fit	cooperative control fixed	cooperative control fit
k_A	0*	0*	0*	0*
k_a	1	1	1	1
k_{IA}	0.000001*	1*	0.366*	1*
n_{IA}	1	1	1.812*	1*
k_B	0*	0*	0*	0.134*
k_b	1	1	1	1
k_{AB}	1.939*	2.234*	17.86*	6.709*
n_{AB}	1	1	6.054*	2.797*
k_{bA}	2	0*	2	0*

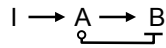
n_{bA}	1	1	1	1*
node A SWRMS	19.83	0	18.4	0
node B SWRMS	19.8	11.09	9.97	3.72
overall SWRMS	19.81	5.546	14.18	1.862
AIC	41.14	22.77	39.80	11.31
rel. robustness	1000	132	227	31
abs. robustness	0	0	0	1.5

Differential equations and steady-state node activities:

$$[\dot{A}] = [a](k_A + k_{IA}[I]^{n_{IA}} + k_{bA}[b]^{n_{bA}}) - [A](k_a) \quad [\dot{B}] = [b](k_B + k_{AB}[A]^{n_{AB}}) - [B](k_b)$$

$$[A] = \frac{k_A + k_{IA}[I]^{n_{IA}} + k_{bA}[b]^{n_{bA}}}{k_A + k_{IA}[I]^{n_{IA}} + k_{bA}[b]^{n_{bA}} + k_a} \quad [B] = \frac{k_B + k_{AB}[A]^{n_{AB}}}{k_B + k_{AB}[A]^{n_{AB}} + k_b}$$

T8 - low-true negative feedforward (push-pull)



parameter	non-coop. control fixed	non-coop. control fit	cooperative control fixed	cooperative control fit
k_A	0*	0*	0*	0*
k_a	1	1	1	1
k_{IA}	1*	1*	1*	1*
n_{IA}	1	1	1*	1*
k_B	0*	0*	0.288*	0*
k_b	1	0*	1	0*
k_{AB}	4.443*	1*	8.035*	1*
n_{AB}	1	1	2.104*	1*
k_{ab}	2	1*	2	1*
n_{ab}	1	1	1	1*
node A SWRMS	0	0	0	0
node B SWRMS	6.37	0	2.937	0
overall SWRMS	3.187	0	1.468	0
AIC	11.91	−∞	3.51	−∞
rel. robustness	110	60	24	7
abs. robustness	0	60	3	7

Differential equations and steady-state node activities:

$$[\dot{A}] = [a](k_A + k_{IA}[I]^{n_{IA}}) - [A](k_a) \quad [\dot{B}] = [b](k_B + k_{AB}[A]^{n_{AB}}) - [B](k_b + k_{ab}[a]^{n_{ab}})$$

$$[A] = \frac{k_A + k_{IA}[I]^{n_{IA}}}{k_A + k_{IA}[I]^{n_{IA}} + k_a} \quad [B] = \frac{k_B + k_{AB}[A]^{n_{AB}}}{k_B + k_{AB}[A]^{n_{AB}} + k_b + k_{ab}[a]^{n_{ab}}}$$

The following analysis shows that this topology yields perfect DoRA. The steady-state activity of node A, from the analysis of topology T1 and using the optimized parameters given here, is identical to the target function, in which the baseline is 0 and the amplitude, EC_{50} , and Hill cooperativity all equal 1. The steady-state activity of node B is

$$[B] = \frac{k_B + k_{AB} [A]^{n_{AB}}}{k_B + k_{AB} [A]^{n_{AB}} + k_b + k_{ab} [a]^{n_{ab}}}$$

Setting the model parameters to those that were found in the optimized results ($k_B = k_b = 0$, $k_{AB} = k_{ab}$, and $n_{AB} = n_{ab} = 1$) simplifies the node B activity to

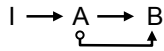
$$[B] = \frac{[A]}{[A] + [a]}$$

We also assumed throughout this work that the total concentration of each node equals one, which further simplifies this equation to

$$[B] = [A]$$

This is the DoRA condition. Furthermore, because the activity of node A was already shown to equal the target function, this shows that the node B activity also equals the target function. Note that the solution only arises if all of the conditions listed above are true. This is the only solution for this model, which implies that the model does not exhibit bistability.

T9 - low-true positive feedforward



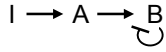
parameter	non-coop. control fixed	non-coop. control fit	cooperative control fixed	cooperative control fit
k_A	0*	0*	0.248*	0*
k_a	1	1	1	1
k_{IA}	1*	1*	0.606*	1*
n_{IA}	1	1	1.442*	1*
k_B	0*	0*	0*	0.134*
k_b	1	1	1	1
k_{AB}	1.529*	2.234*	13.044*	6.709*
n_{AB}	1	1	5.319*	2.797*
k_{aB}	2	0*	2	0*
n_{aB}	1	1	1	1*
node A SWRMS	0	0	4.98	0
node B SWRMS	32.47	11.09	21.57	3.72
overall SWRMS	16.23	5.546	13.28	1.862
AIC	37.96	22.77	38.74	11.31
rel. robustness	263	132	374	30
abs. robustness	0	0	0	1.2

Differential equations and steady-state node activities:

$$[\dot{A}] = [a](k_A + k_{IA} [I]^{n_{IA}}) - [A](k_a) \quad [\dot{B}] = [b](k_B + k_{AB} [A]^{n_{AB}} + k_{aB} [a]^{n_{aB}}) - [B](k_b)$$

$$[A] = \frac{k_A + k_{IA} [I]^{n_{IA}}}{k_A + k_{IA} [I]^{n_{IA}} + k_a} \quad [B] = \frac{k_B + k_{AB} [A]^{n_{AB}} + k_{aB} [a]^{n_{aB}}}{k_B + k_{AB} [A]^{n_{AB}} + k_{aB} [a]^{n_{aB}} + k_b}$$

T10 - negative control arrow



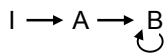
parameter	non-coop. control fixed	non-coop. control fit	cooperative control fixed	cooperative control fit
k_A	0*	0*	0*	0*
k_a	1	1	1	1
k_{IA}	1*	1*	1*	1*
n_{IA}	1	1	1*	1*
k_B	0*	0*	0.164*	0.119*
k_b	1	1	1	1
k_{AB}	4.331*	2.234*	19.498*	8.092*
n_{AB}	1	1	3.218*	2.811*
k_{Bb}	2	0*	2	18.996*
n_{Bb}	1	1	1	7.274*
node A SWRMS	0	0	0	0
node B SWRMS	13.374	11.09	3.62	3.04
overall SWRMS	6.687	5.546	1.81	1.52
AIC	23.77	22.77	6.86	8.06
rel. robustness	247	133	23	23
abs. robustness	0	0	1.2	1.6

Differential equations and steady-state node activities:

$$[\dot{A}] = [a](k_A + k_{IA} [I]^{n_{IA}}) - [A](k_a) \quad [\dot{B}] = [b](k_B + k_{AB} [A]^{n_{AB}}) - [B](k_b + k_{Bb} [B]^{n_{Bb}})$$

$$[A] = \frac{k_A + k_{IA} [I]^{n_{IA}}}{k_A + k_{IA} [I]^{n_{IA}} + k_a} \quad [B] = \frac{k_B + k_{AB} [A]^{n_{AB}}}{k_B + k_{AB} [A]^{n_{AB}} + k_b + k_{Bb} [B]^{n_{Bb}}}$$

T11 - positive control arrow



parameter	non-coop. control fixed	non-coop. control fit	cooperative control fixed	cooperative control fit
k_A	0*	0*	0*	0*
k_a	1	1	1	1

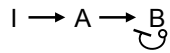
k_{IA}	1*	1*	1*	1*
n_{IA}	1	1	1*	1*
k_B	0*	0*	0*	0.0633*
k_b	1	1	1	1
k_{AB}	0.2733*	2.234*	19.729*	3.7515*
n_{AB}	1	1	8.816*	1.9432*
k_{BB}	2	0*	2	18.8931*
n_{BB}	1	1	1	11.3565*
node A SWRMS	0	0	0	0
node B SWRMS	26.74	11.09	14.598	1.535
overall SWRMS	13.37	5.546	7.299	0.767
AIC	34.85	22.77	29.17	-2.87
rel. robustness	360	134	76	6
abs. robustness	0	0	0	1.6

Differential equations and steady-state node activities:

$$[\dot{A}] = [a](k_A + k_{IA} [I]^{n_{IA}}) - [A](k_a) \quad [\dot{B}] = [b](k_B + k_{AB} [A]^{n_{AB}} + k_{BB} [B]^{n_{BB}}) - [B](k_b)$$

$$[A] = \frac{k_A + k_{IA} [I]^{n_{IA}}}{k_A + k_{IA} [I]^{n_{IA}} + k_a} \quad [B] = \frac{k_B + k_{AB} [A]^{n_{AB}} + k_{BB} [B]^{n_{BB}}}{k_B + k_{AB} [A]^{n_{AB}} + k_{BB} [B]^{n_{BB}} + k_b}$$

T12 - low-true negative control arrow



parameter	non-coop. control fixed	non-coop. control fit	cooperative control fixed	cooperative control fit
k_A	0*	0*	0*	0*
k_a	1	1	1	1
k_{IA}	1*	1*	1*	1*
n_{IA}	1	1	1*	1*
k_B	0*	0*	0.3246*	0*
k_b	1	0*	1	0*
k_{AB}	4.4909*	1*	8.1498*	1*
n_{AB}	1	1	2.1829*	1*
k_{bb}	2	1*	2	1*
n_{bb}	1	1	1	1*
node A SWRMS	0	0	0	0
node B SWRMS	8.157	0	3.526	0
overall SWRMS	4.079	0	1.763	0
AIC	15.86	$-\infty$	6.44	$-\infty$
rel. robustness	96	17	17.48	0.6
abs. robustness	0	17	0.83	0.6

Differential equations and steady-state node activities:

$$\begin{aligned} [\dot{A}] &= [a](k_A + k_{IA} [I]^{n_{IA}}) - [A](k_a) & [\dot{B}] &= [b](k_B + k_{AB} [A]^{n_{AB}}) - [B](k_b + k_{bb} [b]^{n_{bb}}) \\ [A] &= \frac{k_A + k_{IA} [I]^{n_{IA}}}{k_A + k_{IA} [I]^{n_{IA}} + k_a} & [B] &= \frac{k_B + k_{AB} [A]^{n_{AB}}}{k_B + k_{AB} [A]^{n_{AB}} + k_b + k_{bb} [b]^{n_{bb}}} \end{aligned}$$

We investigated this model analytically. The steady-state activity of node A is identical to that given above for topology T1, aligning perfectly with the target function. The steady-state activity for node B is

$$[B] = \frac{k_B + k_{AB} [A]^{n_{AB}}}{k_B + k_{AB} [A]^{n_{AB}} + k_b + k_{bb} [b]^{n_{bb}}}$$

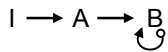
Using the parameters identified in the optimization process ($k_B = k_b = 0$, $k_{AB} = k_{bb}$, and $n_{AB} = n_{bb} = 1$) this simplifies to

$$[B] = \frac{[A]}{[A] + [b]} = \frac{[A]}{[A] + 1 - [B]}$$

$$0 = [B]^2 - [A][B] - [B] + [A] = ([B] - [A])([B] - 1)$$

The factors in the final equality shows that there are two solutions for the node B activity level. They are $[B] = [A]$, which is perfect DoRA, or $[B] = 1$, which is B in its fully active state. This means that if node B is not fully active, then its activity will adjust to become exactly equal to that of node A. However, if node B becomes fully active, either because it was driven there by node A or because of some external influence, then it will get stuck in this state and will not deactivate, independent of the node A activity. This result implies that the node B activity is bistable for all values of $[A]$.

T13 - low-true positive control arrow



parameter	non-coop. control fixed	non-coop. control fit	cooperative control fixed	cooperative control fit
k_A	0*	0*	0*	0*
k_a	1	1	1	1
k_{IA}	1*	1*	1*	1*
n_{IA}	1	1	1*	1*
k_B	0*	0*	0*	0*
k_b	1	1	1	1
k_{AB}	1.0473*	2.234*	20.729*	6.794*
n_{AB}	1	1	7.255*	2.762*
k_{bb}	2	0*	2	0.144*
n_{bb}	1	1	1	0.531*
node A SWRMS	0	0	0	0

node B SWRMS	25.92	11.09	14.648	3.716
overall SWRMS	12.96	5.546	7.324	1.858
AIC	34.35	22.77	29.22	11.28
rel. robustness	343	134	75	31
abs. robustness	0	0	0	1.5

Differential equations and steady-state node activities:

$$[\dot{A}] = [a](k_A + k_{IA}[I]^{n_{IA}}) - [A](k_a) \quad [\dot{B}] = [b](k_B + k_{AB}[A]^{n_{AB}} + k_{bB}[b]^{n_{bB}}) - [B](k_b)$$

$$[A] = \frac{k_A + k_{IA}[I]^{n_{IA}}}{k_A + k_{IA}[I]^{n_{IA}} + k_a} \quad [B] = \frac{k_B + k_{AB}[A]^{n_{AB}} + k_{bB}[b]^{n_{bB}}}{k_B + k_{AB}[A]^{n_{AB}} + k_{bB}[b]^{n_{bB}} + k_b}$$

T14 - positive feedback / low-true negative feedback, arrow to arrow

parameter	non-coop. control fixed	non-coop. control fit	cooperative control fixed	cooperative control fit
k_A	0*	0*	0*	0*
k_a	1	1	1	1
k_{IA}	1*	1*	1*	1*
n_{IA}	1	1	1*	1*
k_B	0*	0.0581*	0.1398*	0.0381*
k_b	1	1	1	1
k_{AB}	1.189*	0*	5.997*	17.491*
n_{AB}	1	1	3.883*	9.326*
k_{ABB}	2	4.2744*	2	2.948*
n_{ABB}	1,1	1,1	1,1	1.659,0*
node A SWRMS	0	0	0	0
node B SWRMS	8.554	6.557	3.729	0.839
overall SWRMS	4.277	3.279	1.864	0.42
AIC	16.62	14.37	7.33	-10.53
rel. robustness	172	92	34	16
abs. robustness	0	0	1.3	9

Differential equations and steady-state node activities:

$$[\dot{A}] = [a](k_A + k_{IA}[I]^{n_{IA}}) - [A](k_a) \quad [\dot{B}] = [b](k_B + k_{AB}[A]^{n_{AB}} + k_{ABB}[A]^{n_{ABB1}}[B]^{n_{ABB2}}) - [B](k_b)$$

$$[A] = \frac{k_A + k_{IA}[I]^{n_{IA}}}{k_A + k_{IA}[I]^{n_{IA}} + k_a} \quad [B] = \frac{k_B + k_{AB}[A]^{n_{AB}} + k_{ABB}[A]^{n_{ABB1}}[B]^{n_{ABB2}}}{k_B + k_{AB}[A]^{n_{AB}} + k_{ABB}[A]^{n_{ABB1}}[B]^{n_{ABB2}} + k_b}$$

T15 - negative feedback / low-true positive feedback, arrow to arrow

	$I \rightarrow A \rightleftharpoons B$ non-coop.	$I \rightarrow A \rightleftharpoons B$ non-coop.	cooperative	cooperative
parameter	control fixed	control fit	control fixed	control fit
k_A	0*	0*	0*	0*
k_a	1	1	1	1
k_{IA}	1*	1*	1*	1*
n_{IA}	1	1	1*	1*
k_B	0*	0*	0*	0.0381*
k_b	1	1	1	1
k_{AB}	1.284*	2.234*	12.018*	2.948*
n_{AB}	1	1	4.832*	1.659*
k_{AbB}	2	0*	2	17.491*
n_{AbB}	1,1	1,1	1,1	9.326,0*
node A SWRMS	0	0	0	0
node B SWRMS	13.016	11.09	2.482	0.839
overall SWRMS	6.508	5.546	1.241	0.419
AIC	23.33	22.77	0.82	-10.55
rel. robustness	288	132	28	17
abs. robustness	0	0	6	10

Differential equations and steady-state node activities:

$$[\dot{A}] = [a](k_A + k_{IA} [I]^{n_{IA}}) - [A](k_a) \quad [\dot{B}] = [b](k_B + k_{AB} [A]^{n_{AB}} + k_{AbB} [A]^{n_{AbB1}} [b]^{n_{AbB2}}) - [B](k_b)$$

$$[A] = \frac{k_A + k_{IA} [I]^{n_{IA}}}{k_A + k_{IA} [I]^{n_{IA}} + k_a} \quad [B] = \frac{k_B + k_{AB} [A]^{n_{AB}} + k_{AbB} [A]^{n_{AbB1}} [b]^{n_{AbB2}}}{k_B + k_{AB} [A]^{n_{AB}} + k_{AbB} [A]^{n_{AbB1}} [b]^{n_{AbB2}} + k_b}$$

T16 - positive feedback / low-true negative feedback, arrow to arrow

	$I \rightleftharpoons A \rightarrow B$	$I \rightleftharpoons A \rightarrow B$	cooperative	cooperative
parameter	control fixed	control fit	control fixed	control fit
k_A	0.0469*	0*	0*	0*
k_a	1	1	1	1
k_{IA}	0*	1*	0.164*	1*
n_{IA}	1	1	0.2027*	1*
k_B	0*	0*	0.161*	0.1345*
k_b	1	1	1	1
k_{AB}	2.1744*	2.234*	3.847*	6.709*
n_{AB}	1	1	2.2848*	2.797*
k_{IBA}	2	0*	2	0*
n_{IBA}	1,1	1,1	1,1	1,1*
node A SWRMS	3.563	0	4.69	0
node B SWRMS	9.689	11.09	5.863	3.724

overall SWRMS	6.626	5.546	5.278	1.862
AIC	23.62	22.77	23.98	13.31
rel. robustness	366	134	282	31
abs. robustness	0	0	0	1.4

Differential equations and steady-state node activities:

$$[\dot{A}] = [a] \left(k_A + k_{IA} [I]^{n_{IA}} + k_{IBA} [I]^{n_{IBA1}} [B]^{n_{IBA2}} \right) - [A] (k_a) \quad [\dot{B}] = [b] \left(k_B + k_{AB} [A]^{n_{AB}} \right) - [B] (k_b)$$

$$[A] = \frac{k_A + k_{IA} [I]^{n_{IA}} + k_{IBA} [I]^{n_{IBA1}} [B]^{n_{IBA2}}}{k_A + k_{IA} [I]^{n_{IA}} + k_{IBA} [I]^{n_{IBA1}} [B]^{n_{IBA2}} + k_a} \quad [B] = \frac{k_B + k_{AB} [A]^{n_{AB}}}{k_B + k_{AB} [A]^{n_{AB}} + k_b}$$

T17 - negative feedback / low-true positive feedback, arrow to arrow

	non-coop. control fixed	non-coop. control fit	cooperative control fixed	cooperative control fit
$I \rightleftharpoons A \rightarrow B$ 				
parameter				
k_A	0*	0*	0*	0*
k_a	1	1	1	1
k_{IA}	0.0247*	1*	0.058*	1*
n_{IA}	1	1	2.576*	1*
k_B	0*	0*	0.0878*	0.1345*
k_b	1	1	1	1
k_{AB}	2.0929*	2.234*	9.049*	6.709*
n_{AB}	1	1	3.338*	2.797*
k_{IBA}	2	0*	2	0*
n_{IBA}	1,1	1,1	1,1	1,1*
node A SWRMS	3.2897	0	5.098	0
node B SWRMS	13.458	11.09	1.5904	3.724
overall SWRMS	8.374	5.546	3.344	1.862
AIC	27.37	22.77	16.68	13.31
rel. robustness	626	131	276	31
abs. robustness	0	0	0	1.6

Differential equations and steady-state node activities:

$$[\dot{A}] = [a] \left(k_A + k_{IA} [I]^{n_{IA}} + k_{IBa} [I]^{n_{IBa1}} [b]^{n_{IBa2}} \right) - [A] (k_a) \quad [\dot{B}] = [b] \left(k_B + k_{AB} [A]^{n_{AB}} \right) - [B] (k_b)$$

$$[A] = \frac{k_A + k_{IA} [I]^{n_{IA}} + k_{IBa} [I]^{n_{IBa1}} [b]^{n_{IBa2}}}{k_A + k_{IA} [I]^{n_{IA}} + k_{IBa} [I]^{n_{IBa1}} [b]^{n_{IBa2}} + k_a} \quad [B] = \frac{k_B + k_{AB} [A]^{n_{AB}}}{k_B + k_{AB} [A]^{n_{AB}} + k_b}$$

T18 - negative feedforward / low-true positive feedforward, arrow to arrow

	$I \rightarrow A \rightleftharpoons B$ 	$I \rightarrow A \rightleftharpoons B$ 	cooperative	cooperative
parameter	control fixed	control fit	control fixed	control fit
k_A	0*	0*	0*	0*
k_a	1	1	1	1
k_{IA}	1*	1*	1*	1*
n_{IA}	1	1	1*	1*
k_B	0*	0*	0*	0.0381*
k_b	1	1	1	1
k_{AB}	1.494*	2.234*	11.726*	17.491*
n_{AB}	1	1	4.757*	9.326*
k_{aAB}	2	0*	2	2.948*
n_{aAB}	1,1	1,1	1,1	0,1.659*
node A SWRMS	0	0	0	0
node B SWRMS	15.277	11.09	2.838	0.839
overall SWRMS	7.638	5.546	1.419	0.420
AIC	25.89	22.77	2.96	-10.53
rel. robustness	225	133	24	27
abs. robustness	0	0	3.7	16

Differential equations and steady-state node activities:

$$[\dot{A}] = [a](k_A + k_{IA}[I]^{n_{IA}}) - [A](k_a) \quad [\dot{B}] = [b](k_B + k_{AB}[A]^{n_{AB}} + k_{aAB}[a]^{n_{aAB1}}[A]^{n_{aAB2}}) - [B](k_b)$$

$$[A] = \frac{k_A + k_{IA}[I]^{n_{IA}}}{k_A + k_{IA}[I]^{n_{IA}} + k_a} \quad [B] = \frac{k_B + k_{AB}[A]^{n_{AB}} + k_{aAB}[a]^{n_{aAB1}}[A]^{n_{aAB2}}}{k_B + k_{AB}[A]^{n_{AB}} + k_{aAB}[a]^{n_{aAB1}}[A]^{n_{aAB2}} + k_b}$$

T19 - positive feedforward / low-true negative feedforward, arrow to arrow

	$I \rightarrow A \rightleftharpoons B$ 	$I \rightarrow A \rightleftharpoons B$ 	cooperative	cooperative
parameter	control fixed	control fit	control fixed	control fit
k_A	0*	0*	0*	0*
k_a	1	1	1	1
k_{IA}	1*	1*	1*	1*
n_{IA}	1	1	1*	1*
k_B	0*	0.0377*	0.1653*	0.0381*
k_b	1	1	1	1
k_{AB}	1.201*	0*	6.797*	17.491*
n_{AB}	1	1	4.166*	9.326*
k_{AAB}	2	4.619*	2	2.948*
n_{AAB}	1,1	1,1	1,1	1.654,0*
node A SWRMS	0	0	0	0
node B SWRMS	7.302	4.794	3.217	0.839

overall SWRMS	3.651	2.397	1.609	0.420
AIC	14.08	9.35	4.97	-10.53
rel. robustness	207	153	47	16
abs. robustness	0	11	4.6	9

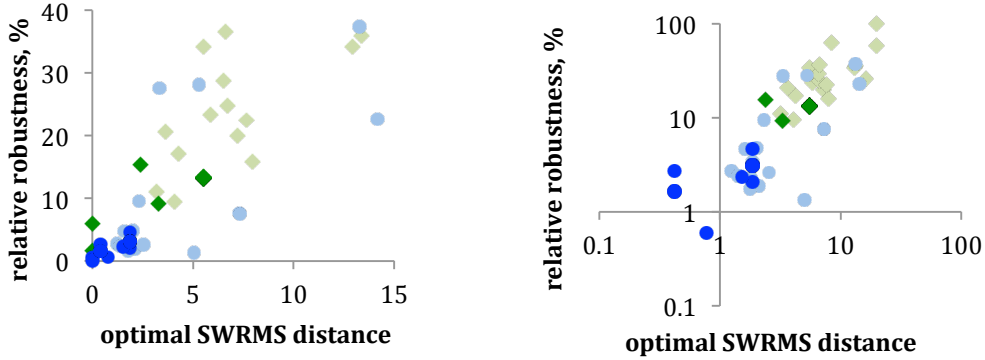
Differential equations and steady-state node activities:

$$[\dot{A}] = [a](k_A + k_{IA}[I]^{n_{IA}}) - [A](k_a) \quad [\dot{B}] = [b](k_B + k_{AB}[A]^{n_{AB}} + k_{AAB}[A]^{n_{AAB1}}[A]^{n_{AAB2}}) - [B](k_b)$$

$$[A] = \frac{k_A + k_{IA}[I]^{n_{IA}}}{k_A + k_{IA}[I]^{n_{IA}} + k_a} \quad [B] = \frac{k_B + k_{AB}[A]^{n_{AB}} + k_{AAB}[A]^{n_{AAB1}}[A]^{n_{AAB2}}}{k_B + k_{AB}[A]^{n_{AB}} + k_{AAB}[A]^{n_{AAB1}}[A]^{n_{AAB2}} + k_b}$$

4.2. Robustness of two-node topologies

To better understand the robustness parameters that we quantified and reported above, we looked for correlations between their values and the optimal SWRMS distances. The following graphs show the relative robustness values. As described above, the relative robustness for a particular model is the percent of trial models that had SWRMS distances less than 3 units greater than the optimal SWRMS distance. This tests the robustness of an optimized model to parameter variation.

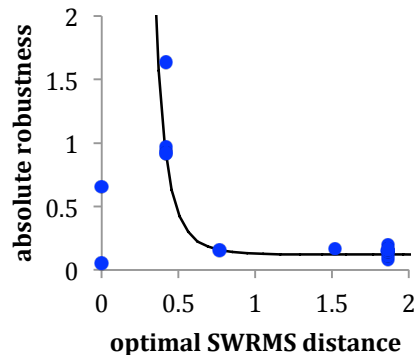


The two graphs present the same data but use either linear and log scales to show the results more clearly. Colors are the same as in Figure 3 of the main text (green for non-cooperative models, blue for cooperative; light colors for fixed control arrows and dark colors for fit control arrows). These graphs show a positive correlation between robustness and optimal SWRMS distance. In these results, the linear topology, T1, and the push-pull topology, T8, are typical; all of their data points lie close to the main diagonal. In particular, the fully optimized push-pull topology has an SWRMS distance of 0 and, correspondingly, a very low robustness of 0.6%. This low robustness shows that it is highly sensitive to parameter variation.

To better understand this correlation, we considered the SWRMS distance as a function of parameter space, visualizing the function as a curved surface. This surface has a depression that is centered around the region where the parameters are optimal, and a minimum at the optimal

parameters. The correlation shows that topologies that produce deep depressions in the SWRMS surface (e.g. the push-pull topology) tend to have narrow depressions, whereas those that produce small depressions in the SWRMS surface tend to have broad depressions.

A somewhat different picture emerges from the absolute robustness values. The absolute robustness is the percent of trial models that had SWRMS distances below a value of 3. This tested the likelihood that a model with randomly chosen parameters would exhibit partial DoRA. The following figure shows that absolute robustness values generally correlate inversely with the optimal SWRMS distance.



As before, blue dots represent the models with both control arrows and cooperativity optimized. Data for models optimized in other ways are not shown for clarity, but generally agreed with the same trend. The line shown here was not fit to the data, but simply added to guide the eye. The two points that do not lie on the line are for T8 (robustness of 0.6), the push-pull topology, and T12 (robustness of 0.06), which also includes a low-true negative arrow and achieves DoRA in a similar manner. The inverse correlation found here shows that, in general, models that are better at exhibiting DoRA also have a greater range of parameters for which they exhibit partial DoRA. Considering the SWRMS surface as a function of parameter space, this shows that the width of a depression at a fixed height above the baseline (SWRMS distance of 0) tends to increase as the depression gets deeper, much as one would expect for a depression that has sloped sides. However, topologies T8 and T12 are exceptions. For them, relatively few randomly chosen parameter sets yielded partial DoRA. This implies that the depressions in their SWRMS surfaces are particularly narrow. This agrees with the results for the relative robustness, where we found that these topologies are particularly sensitive to parameter variation.

4.3. Control arrows act independently

We tested whether any two-node topology with multiple control arrows could produce better DoRA than those with single arrows. To do so, we started with a topology with a single control arrow and then added all control arrows that had produced the same or larger SWRMS distances when used alone. Upon re-optimization, we found that these additional arrows led to negligible improvement in every case (see below). For example, the SWRMS distance for T14 was 3.28 and the distance for the same topology plus control arrows from all single-arrow topologies that produced worse fits was 3.22. This showed that control reactions cannot work in synergy to produce DoRA in two-node models.

The following table presents optimized model parameters for several two-node models that included multiple control arrows. Each of these models used non-cooperative reactions. ‘x’ values in the table represent arrows that were not included in the model. Each column represents one model. The column labeled “T1+worse” is for topology T1, which is the linear topology, plus all control arrows that did not reduce the SWRMS fit distance to below that of T1 when used alone. For example, adding negative feedback to T1, creating topology T2, did not lower the SWRMS fit distance, so it was a “worse” arrow and was included in the “T1+worse” model. On the other hand, adding a low-true negative feedforward to T1, creating topology T8, did lower the SWRMS fit distance, so it was not a “worse” arrow and was not included in this particular model. The other models listed here are analogous. The last rows of the table present the SWRMS fit distances for nodes A and B and for the overall model. The final “control distance” row presents the SWRMS fit distance for the same topology but without any of the “worse” arrows. For example, the control distance for the “T1+worse” model is simply the SWRMS fit distance for topology T1.

parameter	parameter description	T1 +worse	T8 +worse	T12 +worse	T14 +worse	T19 +worse
k_A	A activation	0	0	0	0	0
k_B	B activation	0	0	0	0	0
k_a	A inactivation	1	1	1	1	1
k_b	B inactivation	1	0	0	1	1
k_{IA}	core arrow	1	1	1	1	1
k_{AB}	core arrow	2.234	1	1	0	0
k_{Ba}	in T2, n.fb.	0	0	0	0.045	0
k_{Ab}	in T3, p.fb.	0.203	0	0	0	0
k_{Ab}	in T4, n.ff.	0	0	0	0	0
k_{AB2}	in T5, p.ff.	0	0	0	0	0
k_{ba}	in T6, lt.n.fb.	0.867	0	0	0.031	0
k_{bA}	in T7, lt.p.fb.	0	0	0	0	0
k_{ab}	in T8, lt.n.ff.	x	1	x	x	x
k_{aB}	in T9, lt.p.ff.	0	0	0	0	0
k_{Bb}	in T10, n.	0	0	0	0	0
k_{BB}	in T11, p.	0	0	0	0	0
k_{bb}	in T12, lt.n.	x	0	1	x	x
k_{bB}	in T13, lt.p.	0	0	0	0.067	0.046
k_{ABB}	in T14, p.fb.	x	0	0	4.370	0
k_{AbB}	in T15, n.fb.	0	0	0	0	0
k_{IBA}	in T16	0.203	0	0	0.045	0
k_{IbA}	in T17	0.415	0	0	0.031	0
k_{AaB}	in T18	0	0	0	0	0
k_{AAB}	in T19	x	0	0	x	4.672
node A SWRMS		0	0	0	0	0
node B SWRMS		11.091	0	0	6.449	4.741
overall SWRMS		5.545	0	0	3.225	2.371
comparison SWRMS		5.546	0	0	3.279	2.397

Key to abbreviations in the parameter description column: lt. = low-true, n. = negative, p. = positive, fb. = feedback, and ff. = feedforward.

These results show that control arrows act essentially independently of each other as opposed to acting synergistically. More specifically, if two control arrows do not cause the network to exhibit DoRA by when used separately, then they also do not cause the network to exhibit DoRA when used together. This test investigated all possible pairs of control arrows.

5. Results for four-node topologies

5.1 Idealized target functions

The following table presents the parameters for several 4-node models that we fit to idealized target functions. The main text discusses the models and the left column of Figure 4 presents their dose-response functions.

parameter	parameter description	Figure 4A linear	Figure 4B cooperative	Figure 4C pos. ff.	Figure 4D push-pull	Figure 4E pull reaction
k_A	A activation	0	0	0	0	0
k_B	B activation	0	0.151	0	0	0
k_C	C activation	0	0.177	0	0	0
k_D	D activation	0	0.186	0	0	0
k_a	A inactivation	1	1	1	1	1
k_b	B inactivation	1	1	1	0	1
k_c	C inactivation	1	1	1	0	1
k_d	D inactivation	1	1	1	0	0
k_{IA}	rate, I→A	1	1	1	1	1
k_{AB}	rate, A→B	2.032	6.201	2.234	1	2.041
k_{BC}	rate, B→C	1.858	6.316	0	1	1.866
k_{CD}	rate, C→D	1.784	6.305	0	1	1
n_{IA}	order, I→A	1	1	1	1	1
n_{AB}	order, A→B	1	2.745	1	1	1
n_{BC}	order, B→C	1	2.851	1	1	1
n_{CD}	order, C→D	1	2.880	1	1	1
k_{AC}	p.ff., A→C	x	x	2.234	x	x
k_{AD}	p.ff., A→D	x	x	2.234	x	x
k_{ab}	lt.n.ff., A→B	x	x	x	1	x
k_{bc}	lt.n.ff., B→C	x	x	x	1	x
k_{cd}	lt.n.ff., C→D	x	x	x	1	x
k_{ad}	lt.n.ff., A→D	x	x	x	x	1.046
A SWRMS		0	0	0	0	0
B SWRMS		11.307	3.835	11.091	0	11.286
C SWRMS		16.037	5.526	11.091	0	16.038
D SWRMS		19.040	6.730	11.091	0	6.631
overall SWRMS		11.596	4.023	8.318	0	8.489

5.2 Yeast dose-response data target functions

The following table presents the parameters for several 4-node models that we fit to target functions that we created from experimental yeast dose-response data. These target functions are described in section 1. The main text discusses the models and the right column of Figure 4 presents their dose-response functions.

parameter	parameter description	Figure 4F linear	Figure 4G cooperative	Figure 4H p.ff.	Figure 4I push-pull	Figure 4J push-pull, cooperative
k_R	R activation	0	0	0	0	0
k_G	G activation	0	0	0	0	0.001
k_F	F activation	0.177	0.140	0.198	0.138	0
k_P	P activation	0	0.208	0	0	0.006
k_r	R inactivation	1	1	1	1	1
k_g	G inactivation	1	1	1	0	0
k_f	F inactivation	1	1	1	1	0.018
k_p	P inactivation	1	1	1	0	0
$k_{\alpha R}$	rate, $\alpha \rightarrow R$	0.2	0.2	0.2	0.2	0.2
k_{RG}	rate, $R \rightarrow G$	2.307	8.675	2.336	1	0.790
k_{GF}	rate, $G \rightarrow F$	1.255	0.762	1.167	1.626	0.957
k_{FP}	rate, $F \rightarrow P$	2.015	2.371E5	0	0.461	5232
$n_{\alpha R}$	order, $\alpha \rightarrow R$	1	1	1	1	1
n_{RG}	order, $R \rightarrow G$	1	2.763	1	1	1.306
n_{GF}	order, $G \rightarrow F$	1	0.224	1	1	0.263
n_{FP}	order, $F \rightarrow P$	1	14.258	1	1	18.491
k_{RF}	p.ff., $R \rightarrow F$	x	x	0	x	x
k_{RP}	p.ff., $R \rightarrow P$	x	x	3.444	x	x
k_{rg}	lt.n.ff., $R \rightarrow G$	x	x	x	0.900	0.792
k_{gf}	lt.n.ff., $G \rightarrow F$	x	x	x	0	1.010
k_{fp}	lt.n.ff., $F \rightarrow P$	x	x	x	0.313	0.878
n_{rg}	lt.n.ff. order	x	x	x	1	1.483
n_{gf}	lt.n.ff. order	x	x	x	1	0.036
n_{fp}	lt.n.ff. order	x	x	x	1	9.374
R SWRMS		0	0	0	0	0
G SWRMS		14.236	4.524	14.247	5.212	0.976
F SWRMS		1.274	0.588	1.012	5.861	0.363
P SWRMS		21.698	4.946	9.617	13.987	0.504
overall SWRMS		9.303	2.514	6.219	6.265	0.461

6. Robustness of results to changes in input data, fitting metric, and parameter values

6.1 Robustness to input data and fitting metric

The similarity between our results from target dose-response curves that were perfectly aligned and from the imperfectly aligned experimental data suggested that our results might be reasonably general. In support of this, we found essentially the same results for the 2-node and 4-node idealized models. Furthermore, we found qualitatively identical results in two preliminary studies. In one, we set the amplitude of the *PRM1* node to 0.35 instead of 0.95. In another, we used a different fitting metric, defining it as the root mean squared differences between the parameters of a Hill function fit to the model and the parameters of the target curves (the DoRA-score, described in section 3.2).

6.2 Robustness to parameter variation

We also tested the robustness of optimized models to parameter variation. In each case, we created a set of 10^5 “trial models” by varying the optimal parameters by up to 3-fold. We computed the fraction of these trial models that had SWRMS distances within 3 units of the optimum value (Document S1). From this survey, we found that the models that fit the targets better, such as the push-pull mechanism (T8) were generally more sensitive to parameter variation than those that fit the targets poorly, such as the linear topology (T1). This observation held for all fits to two-node models, including those in which we only fit some of the parameters. Rephrased: if one pictures the value of the SWRMS metric as a surface in parameter space, our results show that deeper minima in this surface are also narrower. This finding suggested that the high sensitivity of the push-pull model arose from the fact that it fit the target function well, as opposed to some particular attribute of its topology.

7. Michaelis-Menten kinetics

7.1 Simplified Michaelis-Menten, linear topology

We defined the simplified Michaelis-Menten approach as the assumption of Henri-Michaelis-Menten kinetics, but without an explicit treatment of enzyme-substrate complexes. The following analysis shows that topology T1 can exhibit perfect DoRA when assuming simplified Michaelis-Menten kinetics.

For convenience, we assumed that there is no uncatalyzed activation of either node A or node B, meaning that $k_A = k_B = 0$. We also assumed first order kinetics, meaning that $n_{IA} = n_{AB} = 0$. Although we assumed in most of our work that the total amount of each species is equal to 1, we did not make that assumption here; instead, we set the total amount of node A to $[A]_{tot.}$ and the total amount of node B to $[B]_{tot.}$. Using these assumptions and the conventional equations for Michaelis-Menten kinetics at steady-state, the net formation rates of A and B are

$$[\dot{A}] = \frac{k_{c,IA} [I][a]}{[a] + K_{M,IA}} - k_a [A] \quad [\dot{B}] = \frac{k_{c,AB} [A][b]}{K_{M,AB} + [b]} - k_b [B]$$

These equations include the new parameters: $k_{c,IA}$ and $k_{c,AB}$ are the Michaelis-Menten catalytic rate constants for activation of node A by I, and activation of node B by A, respectively. Also, $K_{M,IA}$ and $K_{M,AB}$ are the Michaelis constants for these two reactions. At steady-state, both net formation rates equal zero.

Focus first on the node A equation. It is easy to simplify in two limits. First, consider the limit of low saturation, in which $K_{M,IA}$ is much larger than $[A]_{tot.}$. To do so, we defined $k_{IA} = k_{c,IA}/K_{M,IA}$, substituted this into the node A net formation rate equation, and set the result to zero for the steady-state condition, which gave

$$0 = \frac{k_{IA} K_{M,IA} [I][a]}{[a] + K_{M,IA}} - k_a [A]$$

Next, we took the limit that $K_{M,IA}$ is increased towards infinity, which led to

$$0 = k_{IA} [I][a] - k_a [A]$$

This result is identical to the steady-state equation for the simple mass action approach considered in the rest of this work. It shows that the simple mass action approach is consistent with the simplified Michaelis-Menten approach, but makes the assumption of low enzyme saturation (i.e. K_M values are much larger than species concentrations). In section 4.1, we solved this equation to show that node A aligns perfectly with the target function if $k_a = k_{IA} = 1$.

The net formation rate of node A is also easy to simplify in the opposite limit of strong enzyme saturation, in which $K_{M,IA}$ is much smaller than $[A]_{tot.}$. We took this limit by starting with the net formation rate equation again, decreasing $K_{M,IA}$ to zero, and setting the result to zero for the steady-state condition, which yielded

$$0 = k_{c,IA} [I] - k_a [A]$$

This result solves to

$$[A] = \frac{k_{c,A}}{k_a} [I]$$

This is not a Hill function, which implies that the node A activity cannot align with the target dose-response curve in the limit of high enzyme saturation.

We also solved for the steady-state node A activity between these two limits of low and high enzyme saturation. The result is lengthy so we do not present it here. However, importantly, it is not a Hill function. Together, these results show that the node A activity can only agree with its target function, while assuming simplified Michaelis-Menten kinetics, in the limit of low enzyme saturation, which is also the limit that we investigated throughout the rest of this work.

Focus next on the node B equation. It is structurally identical to the node A equation, so it has the same solutions. As a result, we simply present them here rather than re-deriving them. In the limit of low saturation, meaning that $K_{M,AB}$ is much greater than $[B]_{tot.}$, the steady-state equation is

$$0 = k_{AB} [I][b] - k_b [B]$$

This uses the definition $k_{AB} = k_{c,AB}/K_{M,AB}$. As before, this result is identical to the simple mass action approach that we used in the rest of this work, showing again that the simple mass action approach is equivalent to the simplified Michaelis-Menten approach with the assumption of low enzyme saturation. Section 4.1 shows that use of this steady-state equation does not allow the node B activation to align with the target function. The opposite limit of high enzyme saturation, meaning that $K_{M,AB}$ is much less than $[B]_{tot.}$, leads to the solution

$$[B] = \frac{k_{c,AB}}{k_b} [A]$$

Including the total species concentrations changes the equation slightly to

$$\frac{[B]}{[B]_{tot.}} = \frac{k_{c,AB} [A]_{tot.}}{k_b [B]_{tot.}} \frac{[A]}{[A]_{tot.}}$$

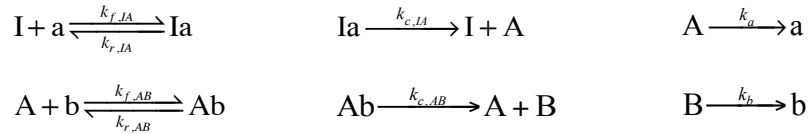
The above equation now shows that the dose-response curve for node B is identical to that for node A, meaning perfect DoRA, if $k_{c,AB}[A]_{tot.} = k_b[B]_{tot.}$. Because we already stated that the node A activity can align perfectly with the target function, this shows that the node B activity can also align perfectly with the target function.

These results show that topology T1 can exhibit perfect DoRA when implemented using simplified Michaelis-Menten kinetics. Topology T1 does so when node A is in the unsaturated limit, where its kinetics are identical to those of the simple mass action approach, and when node B is in the saturated limit. This saturated limit is the “zeroth order regime” described by Goldbeter and Koshland (Goldbeter and Koshland).

7.2 Full Michaelis-Menten, linear topology

This section investigates topology T1 again, but using what the main text labels the “full Henri-Michaelis-Menten” approach. Its only difference from the simplified Michaelis-Menten approach described above is that it treats the enzyme-substrate complexes explicitly.

First, we assumed Henri-Michaelis-Menten mechanisms for both node A activation and node B activation and simulated the resulting reaction network using COPASI. The reaction network was

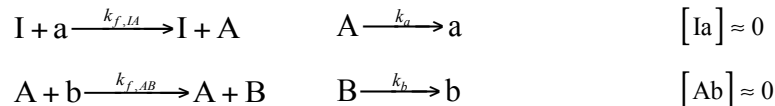


We simulated each of these reactions using mass action kinetics. We also defined the total concentrations for the two species as $[\text{A}]_{tot.}$ and $[\text{B}]_{tot.}$. We defined responses in this case as the total fraction of the active state of each species, independent of whether it was free or part of a complex. We did not have software that would automatically optimize the rate constants in this network, minimizing the SWRMS distance between the network’s steady-state dose-response curves and the target functions, so we did the optimization manually. To do so, we computed steady-state dose-response curves using COPASI, copied the results into an Excel spreadsheet that computed SWRMS distances, and then adjusted parameters and repeated until we found the best possible fit. We followed the greedy random walk approach, described above. This required about 40 iterations, first to identify the best fit and then to verify that it was a local minimum in parameter space. We found that the best fit could arise from many different parameter sets, one of which was: $k_{f,IA} = 1$, $k_{r,IA} = 0$, $k_{c,IA} = 1000$, $k_a = 1$, $k_{f,AB} = 2.234$, $k_{r,AB} = 0$, $k_{c,AB} = 1000$, $k_b = 1$, $[\text{A}]_{tot.} = 1$, and $[\text{B}]_{tot.} = 1$. All of these best fits had a SWRMS distance of 5.55. Inspection of these results showed that all of them were essentially identical to the simple mass action result (leading to the same fit distance) and that they differed from each other in ways that did not affect the dose-response curves (e.g. changing $[\text{A}]_{tot.}$ did not affect the dose-response curves).

To better understand these results, we defined Michaelis constants for the reactions in the usual way,

$$K_{M,IA} = \frac{k_{r,IA} + k_{c,IA}}{k_{f,IA}} \qquad K_{M,AB} = \frac{k_{r,AB} + k_{c,AB}}{k_{f,AB}}$$

In our best fit, $K_{M,IA}$ was much larger than $[\text{A}]_{tot.}$ and $K_{M,AB}$ was much larger than $[\text{B}]_{tot.}$, meaning that both enzymes were in their unsaturated limits. For both Henri-Michaelis-Menten reactions, the reverse rate constant equaled zero and the catalytic rate constant was much larger than the forward rate constant, which made the forward reaction the rate-limiting step. With this identification, the reactions simplify to

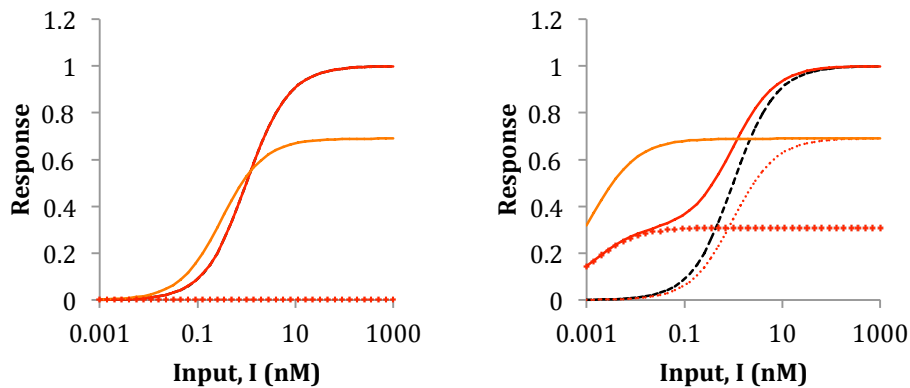


These are exactly the same as the reactions of the simple mass action approach.

Thus, when modeled using the full Henri-Michaelis-Menten approach, topology T1 is best able to exhibit DoRA, meaning that the SWRMS fit distance between its dose-response curves

and the target functions is minimized, when both enzymes are in limit of low enzyme saturation. This solution is identical to the simple mass action approach. This solution is also identical to the simplified Michaelis-Menten approach, when it is considered in this low saturation limit. However, importantly, we found that SWRMS fit distances increased with A enzyme saturation in this full Henri-Michaelis-Menten approach, in marked contrast to the finding that A enzyme saturation can lead to perfect DoRA in the simplified Michaelis-Menten approach.

We further investigated the behavior of this full Henri-Michaelis-Menten approach. To do so, we started by simplifying the reaction network by using simple mass action kinetics for node A, thus effectively fixing the saturation of enzyme I, the input, to a low level. The resulting network is shown in the main text Figure 5B. This simplification did not affect the optimal result at all, but helped us to focus on the interesting behavior, which is the saturation of enzyme A. The following figure shows steady-state dose-response curves from COPASI simulations of this network. On the left, we used essentially the optimal parameters listed above, leading to low enzyme saturation ($k_{IA} = 1$, $k_a = 1$, $k_{f,AB} = 2.234$, $k_{r,AB} = 0$, $k_{c,AB} = 1000$, $k_b = 1$, $[A]_{tot.} = 1$, and $[B]_{tot.} = 1$). On the right, we used parameters for the same node B activation rate but using high enzyme saturation ($k_{IA} = 1$, $k_a = 1$, $k_{f,AB} = 1000$, $k_{r,AB} = 1$, $k_{c,AB} = 2.234$, $k_b = 1$, $[A]_{tot.} = 1$, and $[B]_{tot.} = 1$). In both figure panels, the black dashed line is the target function, the red dotted line is [A], the large red spots are [Ab], the red solid line is total active A which is $[A]+[Ab]$, and the orange line is [B].

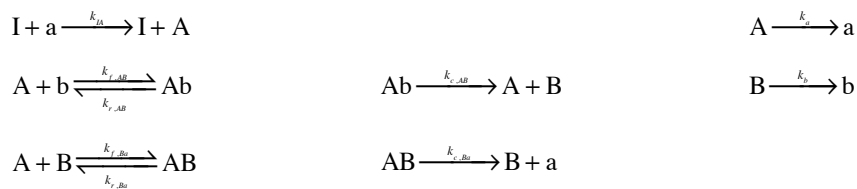


Comparison of these figure panels shows the effects of enzyme saturation. In particular, they show that the activity level of node A changes with the different parameters, despite the facts that the node A parameters are exactly the same in both cases and there is no explicit feedback in topology T1 from node B to node A. We realized that this change arises because the complexation between A and b shifts the equilibrium for node A towards its active state, and that this phenomenon is the same as that described previously as retroactivity or hidden feedback (Ventura et al.); (Del Vecchio et al.). We also realized that this equilibrium shift for node A causes a decrease in the node B EC_{50} , thus worsening its alignment with the target. Furthermore, the complexation sequesters b into Ab complexes, which limits the total activation of node B, seen in the right panel at high input levels.

7.3 Full Michaelis-Menten, topology with negative feedback

We also investigated topology T2, which includes a negative feedback control arrow from node B to node A, using full Henri-Michaelis-Menten kinetics. In this investigation, we treated the activation of node A from the input using simple mass action kinetics, but then explicitly treated all enzyme-substrate complexes for the interactions between nodes A and B. The use of simple mass action kinetics for the activation of A from the input is supported by the findings shown above (section 7.2) that (i) this is identical to its treatment using full Henri-Michaelis-Menten kinetics when taken in the limit of low enzyme saturation, and (ii) when the same reaction in topology T1 was modeled using full Henri-Michaelis-Menten kinetics, it could only fit the target function when in this limit of low enzyme saturation.

This topology T2 reaction network included a positive arrow from node A to node B in which A is the enzyme and b is the substrate. It also included a negative arrow from B to A in which B is the enzyme and A is the substrate. The chemical reactions were



The first row shows activation of A from I and inactivation of A, the second row shows activation of B from A and inactivation of B, and the third row shows negative feedback from B to A. We defined the Michaelis constants for this network in the usual way, with

$$K_{M,AB} = \frac{k_{r,AB} + k_{c,AB}}{k_{f,AB}} \qquad K_{M,Ba} = \frac{k_{r,Ba} + k_{c,Ba}}{k_{f,Ba}}$$

We optimized the rate constants in this reaction network as described in section 7.2. First, by using large $k_{c,AB}$ and $k_{c,Ba}$ values, we imposed low saturation. In this case, optimization led to the same result found with the simple mass action kinetics in which the best result had the negative feedback effectively removed. In this case, the SWRMS distance was 5.55, in agreement with the simple mass action value (section 4.1).

Next, we relaxed this constraint to allow for high enzyme saturation. Further optimization led to a nearly perfect DoRA ($d = 0.118$). The optimal parameter values were: $k_{iA} = 1$, $k_a = 1$, $k_{f,AB} = 4$, $k_{r,AB} = 0$, $k_{c,AB} = 10^5$, $k_b = 1$, $k_{f,Ba} = 10^5$, $k_{r,Ba} = 0$, and $k_{c,Ba} = 1$. For the optimum parameters, $K_{M,AB} = 25,000$ and $K_{M,Ba} = 10^{-5}$. This result shows that the forward arrow from A to B is in the unsaturated limit and the negative feedback arrow from B to A is in the saturated limit. In agreement with this, computations showed that the steady-state concentration of the Ab complex was always essentially zero and the steady-state concentration of the AB complex was always much greater than that of uncomplexed B. In more detail, if there was no input value, then the system had all of node A in the 'a' form and all of node B in the 'b' form. At higher input values, the input converted a to A; the resulting A then enzymatically converted b to B, and then all of the A and B combined into AB complexes. At these intermediate input levels, the a, b, and AB species were highly populated (present in high amounts), while the amounts of the A, B, and Ab species were negligible. Finally, with saturating input, all molecules from both nodes were bound together in AB complexes.

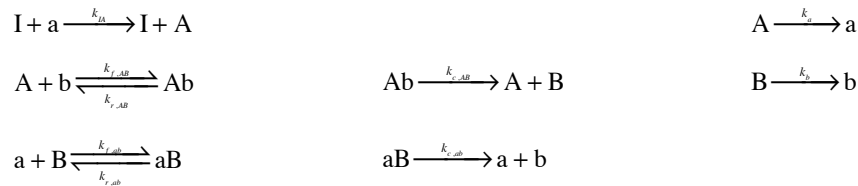
This result showed that essentially perfect DoRA can arise in a reaction network that has a negative feedback loop in it when it is modeled using full Henri-Michaelis-Menten kinetics.

Inspection showed that the negative feedback loop did not act as we had anticipated, by using the signal from node B to decrease the activity of node A. Instead, it acted through tight binding between A and B. This suppressed the formation of B when A values were low and promoted the formation of B when A values were high, both of which promoted alignment of node B with node A.

Another (and complementary) understanding of this network is that it produces DoRA using negative feedback that included a comparator-adjustor mechanism. In this view, tight binding between A and B creates a comparator between A and B amounts. If there is more A than B, then there is unbound A; those A molecules enzymatically convert b to B, thus adjusting the amount of B upwards and reducing the difference between A and B. On the other hand, if there is more B than A, then there is unbound B; those B molecules are not stabilized by the AB complex, so they spontaneously deactivate back to b. This conversion of B to b adjusts the amount of B downwards, again reducing the difference between A and B.

7.4 Full Michaelis-Menten, topology with push-pull

We performed a similar analysis with topology T8, which includes a push-pull mechanism, to see how its steady-state dose-response behavior changes when investigated with full Henri-Michaelis-Menten kinetics. As above in section 7.3, we treated the activation of node A using simple mass action kinetics and treated both arrows between nodes A and B using explicit enzyme-substrate complexes. The chemical reactions for this network are



As before, the first row shows activation of A from I and inactivation of A, and the second row shows activation of B from A and inactivation of B. Here, the third row shows the “pull” reaction, in which ‘a’ acts as an enzyme that converts substrate B to product b. The Michaelis parameters for the two Michaelis-Menten reactions are

$$K_{M,AB} = \frac{k_{f,AB} + k_{c,AB}}{k_{f,AB}} \quad K_{M,ab} = \frac{k_{f,ab} + k_{c,ab}}{k_{f,ab}}$$

As the main text and section 4.1 describe, the push-pull topology can exhibit perfect DoRA when modeled using simple mass action kinetics. Because full Henri-Michaelis-Menten kinetics become identical to simple mass action kinetics in the limit of unsaturated reactions, we anticipated that this network would also exhibit perfect DoRA when both K_M values are large. Indeed, the following rate constants led to essentially perfect DoRA ($d = 10^{-3}$): $k_{IA} = 1$, $k_a = 1$, $k_{f,AB} = 1$, $k_{r,AB} = 0$, $k_{c,AB} = 10^5$, $k_{f,ab} = 1$, $k_{r,ab} = 0$, $k_{c,ab} = 10^5$; using these parameters, $K_{M,AB} = K_{M,ab} = 10^5$.

We wondered whether the same network could also produce DoRA when not in this unsaturated limit. To test this, we tried decreasing the $k_{c,AB}$ and/or $k_{c,ab}$ values in order to increase saturation. Both led to worse fits. Changing the $k_{f,AB}$, $k_{f,ab}$, $k_{r,AB}$, and $k_{r,ab}$ values also led to worse fits. We also tried exploring points in parameter space that were quite distant from this optimum to see if those parameter combinations could produce good DoRA, but again fits

were invariably worse. Finally, we performed optimization from those distant points using the greedy random walk method. We found that the parameters reverted towards the optimum given above. From these results, we concluded that the push-pull mechanism only produces perfect DoRA when all of its reactions are in the unsaturated limit.

8. Negative feedback can produce linear input-output relationships

8.1 General theory

Figure 6A presents a general negative feedback system. This is a standard system that is presented in many control theory textbooks (e.g. (Astrom and Murray, 2008; Franklin et al., 1994)). An operational amplifier that is wired as a voltage follower is a particularly important, and widely studied, instance of this general system (Horowitz and Hill, 1989). Here, we present the mathematics that shows that the output can exactly track the input for this system and what conditions produce this behavior. See control theory (Astrom and Murray, 2008; Franklin et al., 1994) or electronics (Horowitz and Hill, 1989) textbooks for further details.

Define the input value as V_{in} and the output value as V_{out} (for the voltage follower, both values are voltages). Assume that the comparator-adjuster simply computes the difference between the input and output values, multiplies that difference by gain G , and outputs that result. The production of said output may require more power than is available from the input signal; assume that the amplifier has the capability to direct to the output as much power as may be needed. With these assumptions, the output value is equal to the output from the comparator-adjuster, which is

$$V_{out} = G(V_{in} - V_{out})$$

Solving for V_{out} yields

$$V_{out} = \frac{GV_{in}}{G+1}$$

This equation shows that $V_{out} = V_{in}$, meaning that the output exactly tracks the input, in the limit that the gain G approaches infinity, i.e. as the responsiveness of the comparator-adjuster to input-output discrepancies becomes very large. Even with less gain, V_{out} is still directly proportional to V_{in} , but has a lower value.

8.2 Conceptual two-node signaling system with negative feedback

Figure 6B shows a two-node signaling system designed to produce perfect DoRA using feedback and a comparator-adjuster. This system is reasonably similar to the general negative feedback system described above, but has some additional complexities due to the Hill function dependencies of the two nodes.

The steady-state node A activity, assuming simple mass action kinetics and that there is no uncatalyzed activation (see section 2), is

$$\frac{[A]}{[A]_{tot.}} = \frac{k_{IA}[I]}{k_{IA}[I] + k_a}$$

This is a simple Hill function.

We compute the node B activity with two different sets of assumptions. First, to create a system that is mathematically closer to the general negative feedback case, we assume that the output of the comparator-adjuster can be negative as well as positive. This is mathematically simple (but, if the output is molecular, does not make physical sense). With this assumption, the steady-state node B activity follows the same form as the node A activity (and that

presented in section 2, above) but with the forward reaction rate driven by the output of the comparator-adjuster. Consider the comparator-adjuster output as G , the gain factor, times the difference between the comparator-adjuster inputs. With this, the steady-state node B activity is

$$\frac{[B]}{[B]_{tot.}} = \frac{G \left(\frac{[A]}{[A]_{tot.}} - \frac{[B]}{[B]_{tot.}} \right)}{G \left(\frac{[A]}{[A]_{tot.}} - \frac{[B]}{[B]_{tot.}} \right) + k_b}$$

If the gain factor is increased towards infinity, then the k_b term in the denominator becomes irrelevant and so can be dropped. In this limit, this equation simplifies and then factors to yield

$$\begin{aligned} \frac{[B]}{[B]_{tot.}} \left(\frac{[A]}{[A]_{tot.}} - \frac{[B]}{[B]_{tot.}} \right) &= \left(\frac{[A]}{[A]_{tot.}} - \frac{[B]}{[B]_{tot.}} \right) \\ \left(\frac{[A]}{[A]_{tot.}} - \frac{[B]}{[B]_{tot.}} \right) \left(\frac{[B]}{[B]_{tot.}} - 1 \right) &= 0 \end{aligned}$$

This result shows that there are two solutions for the node B activity, which are

$$\frac{[B]}{[B]_{tot.}} = \left\{ \begin{array}{c} \frac{[A]}{[A]_{tot.}} \\ 1 \end{array} \right\}$$

The former solution represents perfect DoRA. The second solution is an artifact of our assumption that the comparator-adjuster output can be negative and that the gain is so large that k_b can be ignored. The important result is that this system can produce perfect DoRA with the assumptions given, provided that the comparator-adjuster produces a highly amplified output. Again, however, if we assume that the output of the comparator-adjuster is molecular, the idea that it can be negative is physically unreasonable.

Due to the need to posit positive values for a molecular output, we revisited this problem again, but with a slightly different comparator-adjuster output. Suppose the output is a gain factor times the difference between the inputs, if this value is positive, and is zero otherwise. In this case, the rate of change of the node B activity is

$$\frac{d[B]}{dt} = G \left\{ \begin{array}{ll} \frac{[A]}{[A]_{tot.}} - \frac{[B]}{[B]_{tot.}} & \text{if } \frac{[B]}{[B]_{tot.}} < \frac{[A]}{[A]_{tot.}} \\ 0 & \text{else} \end{array} \right\} [b] - k_b [B]$$

This dynamical system will have a stable point at the DoRA condition,

$$\frac{[B]}{[B]_{tot.}} = \frac{[A]}{[A]_{tot.}}$$

if $d[B]/dt < 0$ whenever $[B]/[B]_{tot.} > [A]/[A]_{tot.}$ and also $d[B]/dt > 0$ whenever $[B]/[B]_{tot.} < [A]/[A]_{tot.}$. Substituting these conditions into the above rate equation leads to the two following requirements

$$G \left(\frac{[A]}{[A]_{tot.}} - \frac{[B]}{[B]_{tot.}} \right) ([B]_{tot.} - [B]) - k_b [B] > 0 \quad \text{whenever} \quad \frac{[B]}{[B]_{tot.}} < \frac{[A]}{[A]_{tot.}}$$

$$-k_b [B] < 0 \quad \text{whenever} \quad \frac{[B]}{[B]_{tot.}} > \frac{[A]}{[A]_{tot.}}$$

The second condition implies that $k_b > 0$, which is what we were assuming anyhow. The first condition can only be satisfied for all $[B]$ if $G \gg k_b$. With this condition, it is satisfied. The system is physically reasonable because all chemical concentrations are positive. Nevertheless, it is still schematic because we did not specify a biochemical mechanism for the comparator-adjuster.

These results show that that DoRA can arise from a physically reasonable chemical reaction system that uses negative feedback and includes a comparator-adjuster. We intentionally designed this system to be similar to an operational amplifier that is wired as a voltage follower, described above in section 8.1, to show that a similar mechanism could work in biology. There are biological systems in prokaryotes, such as regulation of TetR and controlled genes in transposon Tn10, that operate along these lines, and there is one eukaryotic system that operates at a cellular level, built by human engineers in the past decade and described below. In addition, in this work, we showed above in section 7.3 that topology T2, when modeled with full Henri-Michaelis-Menten kinetics, can also exhibit DoRA using negative feedback and a comparator-adjuster mechanism. It is possible that examination of evolved cellular systems will reveal instances where such feedback control operates.

8.3 A human-built example of linear input-output using negative feedback

Nevozhay et al. (Nevozhay et al., 2009) and Figure 6C, main text, recently engineered a biochemical system that aligns output with input. The system, which mimics the control logic in the bacterial transposon Tn10, operates in yeast cells. It causes expression of the yEGFP fluorophore to vary linearly with the extracellular concentration of anhydrotetracycline (ATc). ATc diffuses into (and out of) yeast cells relatively slowly. ATc binds the tetracycline repressor, TetR, tightly, and on binding inactivates it. This interaction effectively compares the concentration of ATc and TetR. Consider a cell in which, due to an increase in extracellular concentration, intracellular concentration of ATc rises, and becomes greater than that of TetR. Under this condition, all TetR is bound and inactivated, while some ATc is free. Because all TetR is inactivated, expression of yEGFP is not repressed, as it would normally by TetR binding to the two TetR operators (TetOps) in the Tet-repressible promoter that drives yEGFP synthesis. System output, measured by yEGFP signal, therefore increases. In this system, the cells contain TetR because the cells contain a *tetR* gene placed under the control of a second instance of the same Tet-repressible promoter that drives yEGFP. Transcription of *tetR* is now derepressed and the total cellular concentration of TetR monomers increases in parallel with the increase in yEGFP output. Once the total TetR concentration has increased above that of ATc, some TetR monomers are not bound by aTC and are active. This free TetR represses yEGFP expression, capping yEGFP expression (and the total number of active + inactive TetR monomers in the cell,

at a new, higher level. Amplification arises from the fact that a small increase in the number of free TetR monomers brings about a larger decrease in the number of total TetR monomers. A quantitative analysis of this system, presented by the original authors (Nevozhay et al., 2009), presents a description of how negative feedback explains the system's experimentally observed linear input-output relationship.

9. References

Astrom, K.J., and Murray, R.M. (2008). *Feedback systems: an introduction for scientists and engineers* (Princeton: Princeton University Press).

Bajaj, A., Celic, A., Ding, F.-X., Naider, F., Becker, J.M., and Dumont, M.E. (2004). A fluorescent alpha-factor analogue exhibits multiple steps on binding to its G protein coupled receptor in yeast. *Biochem* 43, 13564-13578.

Black, J.W., and Leff, P. (1983). Operational models of pharmacological agonism. *Proc R Soc Lond B* 220, 141-162.

Blumer, K.J., Reneke, J.E., and Thorner, J. (1988). The *STE2* gene product is the ligand-binding component of the alpha-factor receptor of *Saccharomyces crevisiae*. *J Biol Chem* 263, 10836-10842.

Brent, R., and Ptashne, M. (1984). A bacterial repressor protein or a yeast transcriptional terminator can block upstream activation of a yeast gene. *Nature* 312, 612-615.

Burnham, K.P., and Anderson, D.R. (2002). *Model Selection and Multimodel Inference*, 2nd edn (New York: Springer).

Clark, A.J. (1926). The reaction between acetyl choline and muscle cells. *The Journal of Physiology* 61, 530-546.

Clark, A.J. (1933). *The Mode of Action of Drugs on Cells* (Baltimore: The Williams and Wilkins Co.).

Colman-Lerner, A., Gordon, A., Serra, E., Chin, T., Resnekov, O., Endy, D., Pesce, C.G., and Brent, R. (2005). Regulated cell-to-cell variation in a cell-fate decision system. *Nature* 437, 699-706.

Del Vecchio, D., Ninfa, A.J., and Sontag, E.D. (2008). Modular cell biology: retroactivity and insulation. *Molecular Systems Biology* 4, 161.

Franklin, G.F., Powell, J.D., and Emami-Naeini, A. (1994). *Feedback Control of Dynamic Systems*, 3rd edn (Reading, MA: Addison-Wesley Publishing Co.).

Goldbeter, A., and Koshland, D.E.J. (1981). An amplified sensitivity arising from covalent modification in biological systems. *Proc Natl Acad Sci USA* 78, 6840-6844.

Golemis, E.A., and Brent, R. (1992). Fused protein domains inhibit DNA binding by LexA. *Mol Cell Biol* 12, 3006-3014.

Goutelle, S., Maurin, M., Rougier, F., Barbaut, X., Bourguignon, L., Ducher, M., and Maire, P. (2008). The Hill equation: a review of its capabilities in pharmacological modeling. *Fundamental & Clinical Pharmacology* 22, 633-648.

Hartwell, L.H. (1980). Mutants of *Saccharomyces cerevisiae* unresponsive to cell division control by polypeptide mating hormone. *J Cell Biol* 85, 811-822.

Hill, A.V. (1910). The possible effects of the aggregation of the molecules of haemoglobin on its dissociation curves. *Proceedings of the Physiological Society* 40, iv-vii.

Horowitz, P., and Hill, W. (1989). *The Art of Electronics*, 2nd edn (Cambridge: Cambridge Univ. Press).

Huang, C.-Y.F., and Ferrell, J.E.J. (1996). Ultrasensitivity in the mitogen-activated protein kinase cascade. *Proc Natl Acad Sci USA* 93, 10078-10083.

Jenness, D.D., Burkholder, A.C., and Hartwell, L.H. (1983). Binding of alpha-factor pheromone to yeast a cells: chemical and genetic evidence for an alpha-factor receptor. *Cell* 35, 521-529.

Jenness, D.D., Burkholder, A.C., and Hartwell, L.H. (1986). Binding of alpha-factor pheromone to *Saccharomyces cerevisiae* a cells: dissociation constant and number of binding sites. *Mol Cell Biol* 6, 318-320.

Kofahl, B., and Klipp, E. (2004). Modelling the dynamics of the yeast pheromone pathway. *Yeast* 21, 831-850.

Larsen, R.J., and Marx, M.L. (2012). *An Introduction to Mathematical Statistics and Its Applications*, 5th edn (Boston: Prentice Hall).

Moles, C.G., Mendes, P., and Banga, J.R. (2003). Parameter estimation in biochemical pathways: a comparison of global optimization methods. *Genome Research* 13, 2467-2474.

Nevozhay, D., Adams, R.M., Murphy, K.F., Josic, K., and Balázsi, G. (2009). Negative autoregulation linearizes the dose-response and suppresses the heterogeneity of gene expression. *Proc Natl Acad Sci USA* 106, 5123-5128.

Press, W.H., Flanner, B.P., Teukolsky, S.A., and Vetterling, W.T. (1988). *Numerical Recipes in C* (Cambridge: Cambridge University Press).

Schneider, J.J., and Kirkpatrick, S. (2006). *Stochastic Optimization* (Berlin: Springer-Verlag).

Thomson, T.M., Benjamin, K.R., Bush, A., Love, T., Pincus, D., Resnekov, O., Yu, R.C., Gordon, A., Colman-Lerner, A., Endy, D., *et al.* (2011). Scaffold number in yeast signaling system sets tradeoff between system output and dynamic range. *Proc Natl Acad Sci USA* *108*, 20265-20270.

Ventura, A.C., Sepulchre, J.-A., and Merajver, S.D. (2008). A Hidden Feedback in Signaling Cascades Is Revealed. *PLoS Comp Biol* *4*, e1000041.

Yan, L., Ouyang, Q., and Wang, H. (2012). Dose-response aligned circuits in signaling systems. *PLoS ONE* *7*, e34727.

Yi, T.-M., Kitano, H., and Simon, M.I. (2003). A quantitative characterization of the yeast heterotrimeric G protein cycle. *Proc Natl Acad Sci USA* *100*, 10764-10769.

Yu, R.C., Pesce, C.G., Colman-Lerner, A., Lok, L., Pincus, D., Serra, E., Holl, M., Benjamin, K., Gordon, A., and Brent, R. (2008). Negative feedback that improves information transmission in yeast signalling. *Nature* *456*, 755-761.